nature chemistry

ARTICLES

PUBLISHED ONLINE: 31 AUGUST 2014 | DOI: 10.1038/NCHEM.2041

Low-energy spectrum of iron–sulfur clusters directly from many-particle quantum mechanics

Sandeep Sharma[1], Kantharuban Sivalingam[2], Frank Neese[2] and Garnet Kin-Lic Chan[1]*

Iron–sulfur clusters are a universal biological motif. They carry out electron transfer, redox chemistry and even oxygen sensing, in diverse processes including nitrogen fixation, respiration and photosynthesis. Their low-lying electronic states are key to their remarkable reactivity, but they cannot be directly observed. Here, we present the first ever quantum calculation of the electronic levels of [2Fe–2S] and [4Fe–4S] clusters free from any model assumptions. Our results highlight the limitations of long-standing models of their electronic structure. In particular, we demonstrate that the widely used Heisenberg double exchange model underestimates the number of states by one to two orders of magnitude, which can conclusively be traced to the absence of Fe $d \rightarrow d$ excitations, thought to be important in these clusters. Furthermore, the electronic energy levels of even the same spin are dense on the scale of vibrational fluctuations and this provides a natural explanation for the ubiquity of these clusters in catalysis in nature.

Metals in enzymes perform remarkable chemistry under ambient pressures and temperatures. Among the most important cofactors are the iron–sulfur clusters, comprising one to eight Fe atoms bridged by S ligands. In central processes of life ranging from nitrogen fixation to photosynthesis and respiration[1], these clusters perform diverse functions: redox chemistry, electron transfer and even oxygen sensing. Their electronic structure, with multiple low-lying states with differing electronic and magnetic character, holds the key to this rich chemistry. However, uncovering the electronic structure has been highly non-trivial. Direct experimental assignment of these electronic levels in larger clusters has been impossible, because they lie at low energies and can be embedded within the vibrational modes of the clusters[2,3].

Nonetheless, through intense collaboration in the last decades between experiment and theory, a consensus description of FeS cluster electronic states has emerged. This is based on the Heisenberg double exchange (HDE) model, combining Heisenberg exchange between Fe spins with a simplified version of Anderson's double exchange[4,5] for mixed valence delocalization. The HDE model was first proposed by Girerd[6] and Noodleman *et al.*[7,8] for [2Fe–2S] dimers, and then generalized to [3Fe–4S] and [4Fe–4S] clusters by Girerd, Münck and co-workers[9,10], with further extensions in recent years[11,12]. The HDE model has yielded many important insights. For example, the observed electron paramagnetic resonance (EPR) $g < 2$ in reduced [2Fe–2S] dimers was puzzling until it was recognized that the ground state contains antiferromagnetic coupling of the Fe^{II} and Fe^{III} centres[13,14]. Similarly, in [3Fe–4S] and [4Fe–4S] clusters, HDE model mixed valence eigenstates provided the basis to interpret the distinctive Mössbauer, NMR and electron-nuclear double resonance (ENDOR) spectra[15–20].

Despite the many successes of this phenomenological model, its limitations are also well known. The HDE model posits couplings *a priori*, which must be fitted before making predictions. In basic versions, couplings consist of Heisenberg exchange *J*s and double-exchange *B*s, whereas extended versions include anisotropy, zero-field splitting and further contributions[21]. An unambiguous determination of all parameters from experiments is clearly difficult, if not impossible. For example, in one famous case of a [4Fe–4S] cluster[1], the experimentally fitted *B*s range from $\sim$10 cm^{-1} to $\sim$600 cm^{-1}, over two orders of magnitude. Furthermore, FeS couplings obtained from broken-symmetry density functional theory (BS-DFT) computations (for example, in pioneering work by Noodleman and others[8,22–27]) are not clearly more reliable. This is because BS-DFT only describes a weighted average over the (multiplet) states; individual parameters must once again be obtained through fitting, and they also depend strongly on the density functional approximation used[28]. Beyond the above issues, a deeper criticism of the phenomenological models is that they make *a priori* choices about relevant chemical processes; for example, a pure Heisenberg model will completely omit charge transfer phenomena. Without a reliable route to obtain model parameters, we cannot verify their validity, which raises the following troubling question: How can we be sure that the current models are even qualitatively correct?

In principle, it should be possible to compute the states of the FeS clusters directly, without assuming an intermediate model. After all, the long-standing premise of *ab initio* computation is that any molecule's electronic structure is obtainable, without assumptions, from the many-electron Schrödinger equation. Clearly, this has not yet been achieved for FeS clusters. Quantum-mechanical computation is exponentially harder than classical simulation, because it supports superposition and non-local correlations known as entanglement. To avoid this complexity, practical simulations—for example those using DFT—rely on a mean-field approximation, which treats only classical-like quantum states without entanglement. This approximation completely fails in FeS clusters, however, because of the Fe *d*-shells, which are near-degenerate on the Coulomb interaction scale (so-called strongly interacting), rendering the molecular orbital picture and concept of a single mean-field electronic configuration invalid. This is why BS-DFT calculations, the standard computational method applied to FeS clusters, only provide an energetic average over the spectrum and do not allow us to directly obtain the individual electronic states.

A strongly interacting electronic structure fundamentally involves entangled superpositions of many valence configurations. Malrieu and co-workers[29–32] showed that the main classes of configurations for metal centres include the configurations involving

[1]Department of Chemistry, Princeton University, Princeton, New Jersey 08544-1009, USA, [2]Max Planck Institute for Chemical Energy Conversion, 45470 Mülheim, Germany. *e-mail: gkchan@princeton.edu

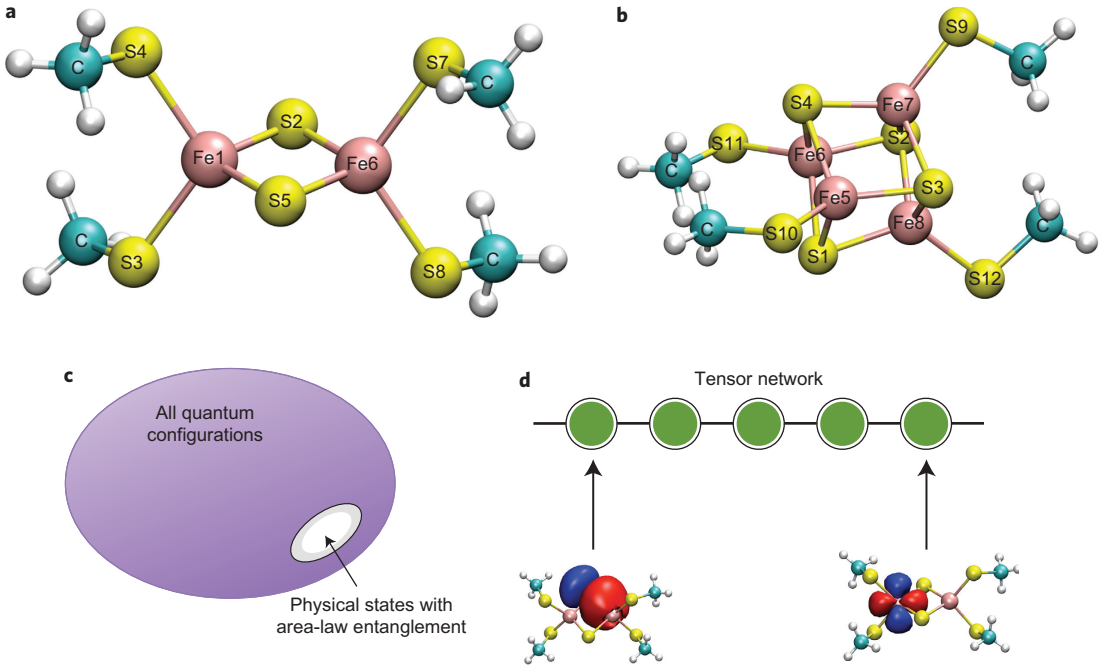

Figure 1 | Model clusters and many-electron wavefunctions used in this work. a,**b**, [2Fe-2S] (**a**) and [4Fe-4S] (**b**) clusters in this work. White circles denote H atoms. (Labels correspond to coordinates in Supplementary Tables 1, 2 and 11.) **c**, Area-law entanglement of the physical states can be used to reduce the complexity of quantum calculations. **d**, Wavefunctions with area-law entanglement can be written compactly as a tensor network where each tensor (represented here by a circle) denotes an active space orbital and the bonds between adjacent orbitals introduce local entanglement between them. The network shown here is the linear network used by the DMRG, which removes the need to model unphysical entanglement between widely separated sites on the chain.

metal *d* electrons (a complete active space, CAS), augmented with excitations of bridging ligand orbitals, or by including ligand orbitals in the active space. However, even with these restrictions, the number of configurations grows exponentially with the number of atoms and quickly becomes intractable. Early attempts to model these superpositions in the [2Fe–2S] dimer had to make further drastic approximations, completely removing non-bridging atoms and including only *d* electrons in the active space[33]. In a [4Fe–4S] cluster, the minimal CAS comprises all Fe 3*d* and S 3*p* valence shells, a distribution of 54 electrons in 36 spatial orbitals, or 1×10^{16} configurations, unmanageable on any computer.

Recent advances from quantum information and condensed matter theory demonstrate, however, that physical quantum states —the quantum states seen in nature—are special and contain a hidden structure to their wavefunctions. In particular, the low energy states possess area-law entanglement[34], reflecting the locality present in all physical systems regardless of interaction strength (Fig. 1c). This structure implies that the coefficients of the valence configurations in the FeS clusters are related in a special way and the information compressed. To encode this relationship we write the wavefunction as a tensor network[35], of which the density matrix renormalization group (DMRG) of White[36], a linear tensor network, is the most widely used example. A tensor in a tensor network represents a local variational degree of freedom. In a molecule, a tensor might represent an atom or an orbital, and contraction of the tensors creates the local entanglement, similar to a bond (Fig. 1d). The area-law implies that if we restrict ourselves to the physically relevant sector of quantum states the tensors used to describe physical states can be of low rank. Working with low-rank tensor networks, we can elevate quantum simulations from the mean-field level to the level of the entangled quantum mechanics necessary to describe FeS clusters, while significantly ameliorating, or in some cases completely bypassing, the exponential complexity of the general quantum-mechanical formulation.

Starting with the work of White and Martin[37], our group and others have been developing tensor networks and the DMRG in the context of quantum chemistry[38–46]. Here, we show that using our *ab initio* DMRG methodology, we can now numerically solve the valence many-particle quantum-mechanical equations for FeS clusters to chemical precision. This allows us, for the first time, to directly compute and probe the individual states and spectra in FeS clusters as large as the [2Fe–2S] and [4Fe–4S] clusters. This direct computation unshackles the discussion of FeS electronic structure from any earlier model assumptions. As will be seen, our calculations enable us to review, revisit and ultimately substantially revise the historical models that have so far been the only basis for understanding electronic structure in these clusters, opening up the possibility to unlock the secrets of the chemistry of these clusters from direct simulation.

Results and discussion

[2Fe–2S] dimers. We consider the synthetic $[Fe_2S_2(SCH_3)_4]^{2-/3-}$ complexes[47] that mimic the dimers prominently found in ferredoxins[48,49] (Fig. 1a).

In canonical understanding based on the HDE model, the Fe atoms are placed in definite valence states. For the oxidized $[2Fe–2S]^{2-}$ dimer, both Fe atoms are assumed high-spin Fe^{III} ($S_{1,2} = 5/2$), whereas for the reduced $[2Fe–2S]^{3-}$ dimer, one is high-spin Fe^{II} ($S_1 = 2$) and the other high-spin Fe^{III} ($S_2 = 5/2$). In the oxidized dimer there is assumed to be no double exchange, and the HDE model reduces to the simpler Heisenberg form,

$$H = 2JS_1 \cdot S_2 \qquad (1)$$

with levels $E(S) = JS(S + 1)$ (S is total dimer spin and J is exchange coupling). In [2Fe–2S] dimers, $J > 0$, so the ground state is low-spin with maximal antiferromagnetic alignment.

In the canonical picture of the reduced dimer, the additional electron can delocalize between the two Fe centres. (This is

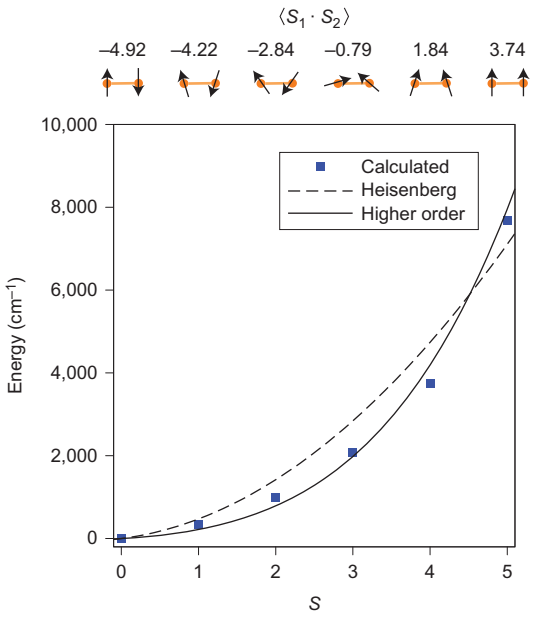

Figure 2 | *Ab initio* levels of $[Fe_2S_2(SCH_3)_4]^{2-}$ and corresponding model fits. The dashed line represents a fit to the Heisenberg model and the solid line a fit to the Heisenberg model plus quadratic couplings, capturing charge fluctuation effects. Top: expectation values of spin-correlation $\langle S_1 \cdot S_2 \rangle$ for increasing dimer spin, showing progression from antiferromagnetic to ferromagnetic ordering.

influenced by geometry and solvation; see, for example, Supplementary Section 1.3 and refs 10 and 50.) In the HDE model[51,52], this electron is placed in either a single bonding-type or antibonding-type orbital between the centres, splitting each Heisenberg level by a double-exchange contribution $B/(S+1/2)$ and giving levels of the form

$$E(S) = JS(S+1) \pm B(S+1/2) \quad (2)$$

As discussed by Noodleman and Baerends[7], double exchange stabilizes high-spin states.

We now examine the accuracy of these existing pictures by comparing against the electronic levels that can now be directly calculated using the *ab initio* DMRG (for details see Supplementary Sections 1.1 and 1.2 and Methods). Figure 2 shows the computed levels of the oxidized $[2Fe–2S]^{2-}$ complex as compared to the predictions of the Heisenberg model (equation (1)). The exact DMRG levels qualitatively form a spin ladder from $S=0$ to $S=5$, in general agreement with the Heisenberg model. As S increases, the spin–spin correlation $\langle S_1 \cdot S_2 \rangle$ increases, transitioning from antiferromagnetic to ferromagnetic alignment. Fitting to equation (1) yields $J \approx 236$ cm^{-1}, which compares reasonably well to fits from magnetic susceptibility measurements on a similar synthetic dimer ($J \approx 148 \pm 16$ cm^{-1}, ref. 51) and computed BS-DFT estimates ($J \approx 310$ cm^{-1}, ref. 52). However, our *ab initio* levels also show significant deviations from the level structure assumed by the traditional Heisenberg model. For example, the Heisenberg model overestimates the lower spin state energies, while underestimating those of the higher spin states. Measuring the local spin on the Fe atoms in our calculations we find $\langle S_1^2 \rangle$ ranges from 5.47 to 5.74 (for the $S=0$ and $S=5$ states, respectively), as compared with $\langle S_1^2 \rangle = 8.75$ for the pure Fe^{III} ($S=5/2$) ion assumed in the model. This deviation from a pure $S=5/2$ ion illustrates the Heisenberg model's limits, which does not allow for additional spin or charge configuration mixing. In fact, charge fluctuations are responsible for the important spin delocalization onto the sulfur orbitals, as previously observed by Noodleman[52]. Guihery and co-workers have derived the form of the corrections to the Heisenberg model that arise from quantum charge fluctuations[12]. In dimers, this yields a quadratic spin coupling $4J_Q(S_1 \cdot S_2)^2$, and fitting to the *ab initio* DMRG levels gives $J \approx 98$ cm^{-1} and $J_Q \approx 6$ cm^{-1}. As demonstrated in Fig. 2, the quadratic coupling greatly improves the agreement, showing the importance of these corrections.

We now turn to the reduced $[2Fe–2S]^{3-}$ dimer. Whereas the disagreement between the standard HDE model and the directly computed *ab initio* spectrum for the oxidized dimer was primarily quantitative, for the reduced dimer the discrepancies are more severe. The HDE model predicts the splitting of the two lowest levels to increase with total spin, $2B(S+1/2)$. However, in the *ab initio* spectrum (Fig. 3a, red curves) the splitting decreases with dimer spin from $S=1/2$ to 3/2. Clearly, this cannot be reproduced by any HDE model parameters, as the splitting is always proportional to S; this remains after geometry relaxation, which introduces trapping (Supplementary Section 1.)

That the earlier model description breaks down for highly excited states is natural, but that it already fails for the lowest two states is surprising. As explained further in the following, this reflects the complicated nature of double exchange in nearly orbitally degenerate metal ions. The HDE model assumes that the additional hopping electron is held in a single pair of prescribed bonding and antibonding orbitals bridging the sulfur ligands. This is appropriate if ligand–field splitting places other bonding and antibonding orbitals at higher energies (Fig. 4a), but is not in fact the case for tetrahedrally coordinated Fe^{III} ions where both orbitals of e-parentage (in T_d symmetry) are near-degenerate, and weak ligand–field splitting by π-donor ligands leads to higher-lying orbitals of t_2-parentage also being accessible for double exchange (Fig. 4b).

The multi-orbital nature of Fe double exchange is immediately seen in the level spectrum at each dimer spin S (Fig. 3). Especially for $S=1/2$, 3/2 and 5/2, the separation between the first two states and the higher states is small, rendering the single pair HDE model completely invalid. Instead, the lowest ten levels constitute a dense manifold of related states, where the hopping electron occupies any one of ten available d orbitals on the Fe atoms.

Multi-orbital double exchange explains many of the earlier difficulties in determining consistent double-exchange parameters from experiment. Simply put, a well-defined global B does not exist. Fitting the two lowest curves to the HDE model yields $J \approx 67$ cm^{-1} and $B \approx 63$ cm^{-1}, while fitting the lowest and highest curves in the manifold yields $J \approx 311$ cm^{-1} and $B \approx 1{,}052$ cm^{-1}. This wide range in B values is consistent with earlier experimental fits, which also yield B couplings varying by a factor of 50 or more[1]. (For a careful analysis of experimental variation in B, see ref. 50).

A naive way to extend the canonical HDE model to include multi-orbital exchange is to assume that the HDE energy levels in equation (2) simply generalize from one to five hopping pairs and five sets of J_i and B_i, $i=1\ldots5$ couplings, with ligand-field splittings Δ_i, $i=1\ldots4$. (Multi-pair HDE models have been considered for [4Fe–4S] clusters in the context of delocalization pathways via σ and δ MO orbitals.) This gives levels of the form

$$E_i(S) = \Delta_i + 2J_i S_1 \cdot S_2 \pm B_i\left(S_i + 1/2\right) \quad (3)$$

where i labels the orbital pair associated with the hopping. Fits to this multi-pair form are shown in Fig. 3b. The multi-pair HDE model does capture the low-lying spectrum better, because it has more parameters, but it still cannot reproduce the non-monotonic behaviour in pairs of energy levels, such as the decreasing gap between the first two levels. This shows that multi-orbital exchange cannot be considered a simple pairwise process.

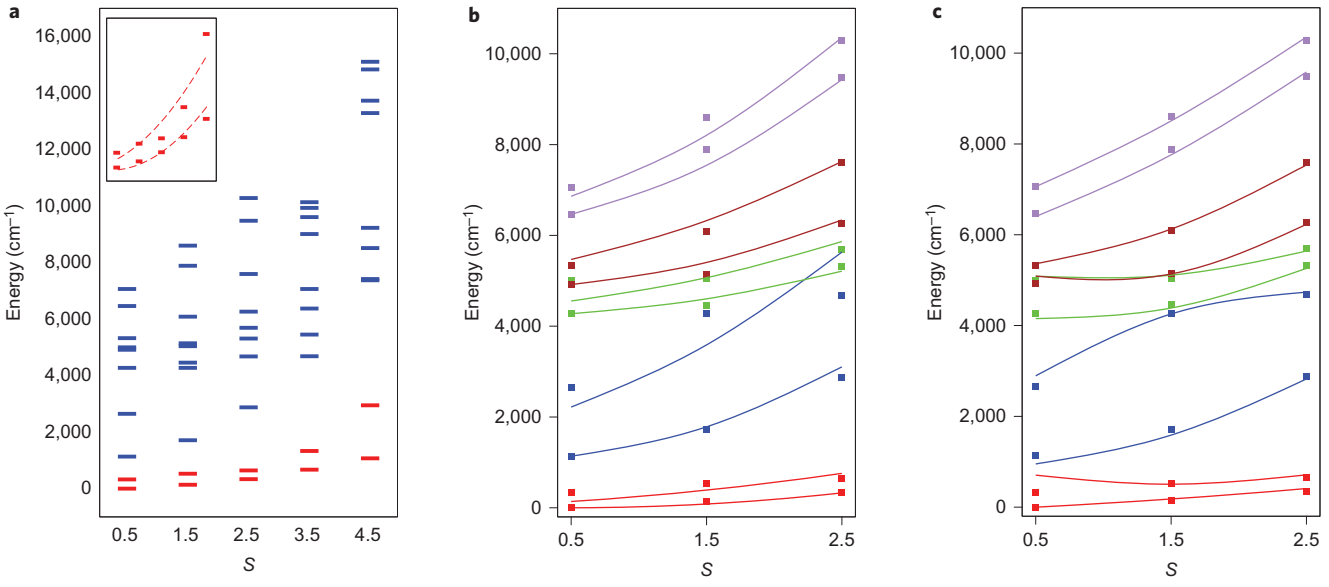

Figure 3 | *Ab initio* levels of $[Fe_2S_2(SCH_3)_4]^{3-}$ and corresponding model fits. The multi-orbital Anderson model proposed here produces an excellent fit to all levels, capturing the essential physics of the low energy states, while the single-pair and multi-pair HDE models do not. **a**, *Ab initio* levels of $[Fe_2S_2(SCH_3)_4]^{3-}$ for each dimer spin *S*. Inset: fit of the lowest two levels (red) to the HDE model. The level separation does not increase monotonically as required in the HDE model, and the separation between the lowest two and higher levels is small (especially for $S = 1/2, 3/2, 5/2$), indicating that the HDE model assumptions break down and multi-orbital double exchange is important. **b**, Fits ($S = 1/2, 3/2, 5/2$) to a multi-pair HDE model. Pairs of corresponding bonding and antibonding states are represented by the same colour. **c**, Fits ($S = 1/2, 3/2, 5/2$) to a multi-orbital Anderson model. **b** and **c** use the same number of parameters, but **c** is much better than **b**, demonstrating that multi-orbital double exchange is not a sum of single exchange processes, as required by the multi-pair HDE model.

The correct qualitative picture for multi-orbital exchange requires a return to Anderson's original Hamiltonian for double exchange. For this system it takes the form (for a detailed derivation see Supplementary Section 1.4)

$$H = \sum_i J_i s_{1i} \cdot s_{2i} + \sum_{i\sigma} \left[\beta_i (c^{\dagger}_{1i\sigma} c_{2i\sigma} + c^{\dagger}_{2i\sigma} c_{1i\sigma}) + \Delta_i (c^{\dagger}_{1i\sigma} c_{1i\sigma} + c^{\dagger}_{2i\sigma} c_{2i\sigma}) \right] \quad (4)$$

(*i* labels *d* orbitals, s_{1i} and s_{2i} are electron spins, and $c^{(\dagger)}_{1i}$ and $c^{(\dagger)}_{2i}$ create and destroy electrons). Note that this Anderson Hamiltonian has the same number of parameters as a multi-pair HDE model (equation (3)), but the fit (Fig. 3c) is much improved and now obtains the correct non-monotonic features. Furthermore, the fit is stable, near unique and yields reasonable parameters: ligand field splittings are ~4,000–5,000 cm^{-1}, consistent with spectroscopic estimates for tetrahedral Fe (Supplementary Table 10). Thus, all qualitative features of our *ab initio* spectrum can be understood by treating multi-orbital exchange in this more complete way.

In summary, our directly computed levels show that the low-lying spectrum of [2Fe–2S] dimers is much richer and denser than the simple pair-splitting long assumed within the canonical HDE picture; the level spectrum is generated by a complex multi-orbital exchange process and this process cannot be viewed as a simple 'sum' over single orbital double-exchange pathways.

[4Fe-4S] clusters. We now turn from FeS dimers to the more complicated [4Fe–4S] clusters. As a representative of nature's cubanes we consider the $[Fe_4S_4(SCH_3)_4)]^{2-}$ cluster, derived from the synthetic cluster studied by Holm and co-workers[53]. The deduction of the cubane ground state from experimental measurements is an early triumph of inorganic spectroscopy[19]. It is conventionally believed that the ground state consists of two coupled iron dimers, located on opposite faces of the cube. The dimers are thought of as mixed-valence $Fe^{2.5+}$, $Fe^{2.5+}$ pairs coupled to a high-spin $S = 9/2$ state, which further recouple in the ground state to form an overall singlet.

Because we can compute the electronic structure of the [4Fe–4S] cluster directly (see Methods) we can now test the long-standing

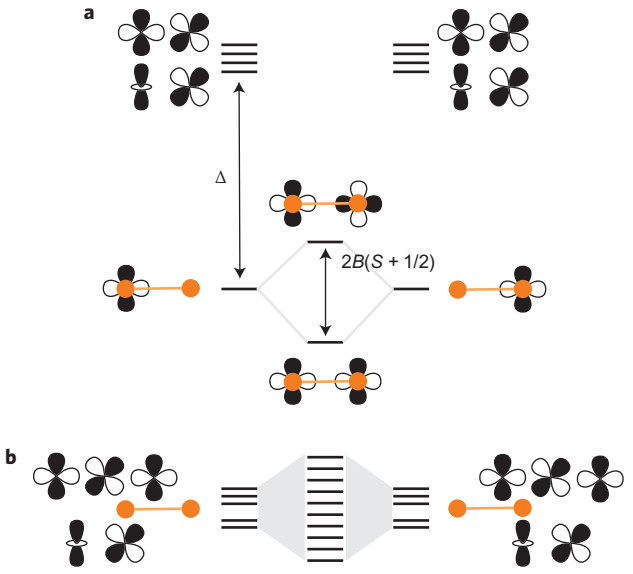

Figure 4 | Origin of the dense manifold in the reduced dimer. Although the HDE model predicts two low-lying states in the reduced dimer, the observed dense manifold can result from a ligand field splitting that is energetically comparable to the hopping energy. **a**, The HDE model assumes that a single electron hops between a pair of *d* orbitals on the Fe ions. This is valid if Δ is sufficiently large that other *d* orbitals are well separated. **b**, In FeS systems, Δ is comparable to the hopping energy, giving a whole manifold of low-lying states at each dimer spin.

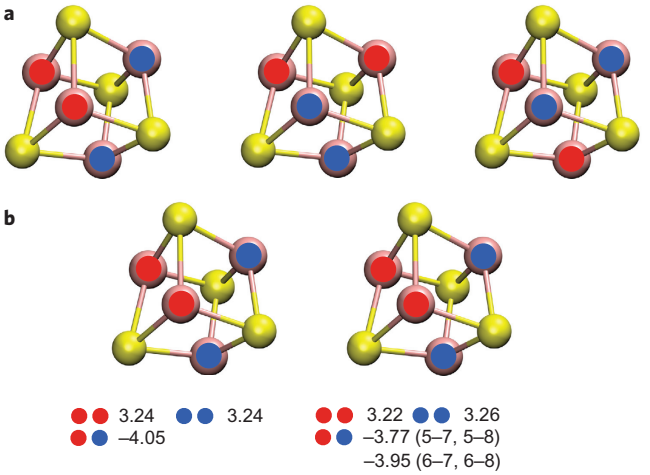

Figure 5 | Spin pairings in the [4Fe–4S] cluster. Unlike in a perfectly cubic cluster, where three equivalent pairings of Fe exist, the geometry-optimized cluster breaks this symmetry and favours one pairing over the other two. The dimer pairs and their relative spin orientations can be detected through the spin correlation functions. **a**, Three equivalent pairings of Fe into dimers in a perfect [4Fe–4S] cubane: red–red, ferromagnetic coupling; red–blue, antiferromagnetic coupling. **b**, Spin correlation functions $(\langle S_i \cdot S_j \rangle)$ for lowest singlet (left) and triplet (right) states of the $[Fe_4S_4(SCH_3)_4]^{2-}$ cluster. The numbers in parenthesis refer to the spin correlation functions established between iron atoms following the atom-numbering nomenclature set up in Fig. 1.

hypothesis for the ground state. In our computed singlet ground state, the spin density is zero everywhere (because our wavefunction is a true spin singlet), but the nature of the couplings can be established from spin correlation functions $\langle S_i \cdot S_j \rangle$ (Fig. 5). These indicate ferromagnetic coupling along the top and bottom faces, with antiferromagnetic coupling between the faces, corresponding precisely to the experimental picture of two high-spin $Fe^{2.5+}$, $Fe^{2.5+}$ dimers recoupled into a singlet, thus confirming the long-standing interpretation. We can further extend our calculations to the lowest triplet state. This lies approximately 350 cm^{-1} above the singlet state. From its spin correlation functions, we see that the triplet corresponds to a spin-canted state, where the $S = 9/2$ dimer spins are tilted relative to their ground-state orientation.

What about the complete [4Fe–4S] spectrum? From the complexity of the [2Fe–2S] spectrum, we expect this will be a formidable beast. While the complete spectrum is too expensive, we can calculate some of the lower-lying states. The ten lowest singlet $S = 0$ and high-spin $S = 9$ states are shown in Fig. 6, as well as the lowest triplet and a (more qualitative) spectrum for the 150 lowest $S = 9$ states. In a perfect cubane we expect three degenerate singlet ground states from the three possible spin couplings in Fig. 5. However, vibronic coupling distorts the ground state of the [4Fe–4S] cluster, opening a gap between the ground and higher-lying states. Nevertheless, even in the distorted [4Fe–4S] cluster, the manifold of low-lying states remains accessible and dense on the 10–20 kcal mol^{-1} scale of biological FeS reorganization energies[54]. A detailed analysis of the [4Fe–4S] excited states and their coupling to distortions is presented in Supplementary Section 2.4. Furthermore, the structure of the low-lying spectrum, for any cluster spin S, is very different to the isolated four low-lying levels predicted by canonical HDE models for each S. This is expected, because the model fails already in the [2Fe–2S] dimers due to the neglect of multi-orbital double exchange discussed above. Appropriate model Hamiltonians for the [4Fe–4S] clusters are analysed in detail in Supplementary Section 2.4.

The high density of states (and their sensitivity to geometry via vibronic coupling) provides an intriguing hypothesis behind the unusual chemical flexibility and ubiquity of the [4Fe–4S] clusters. Conventionally, molecular reactivity proceeds via well-defined potential energy surfaces. However, in [4Fe–4S] clusters, a large number of states of the same (and different) spin are energetically accessible during reorganization dynamics. This suggests that [4Fe–4S] clusters can non-adiabatically switch between many different frontier electronic states in a reaction, in essence a generalization of two-state reactivity already postulated in single-Fe porphyrins[55]

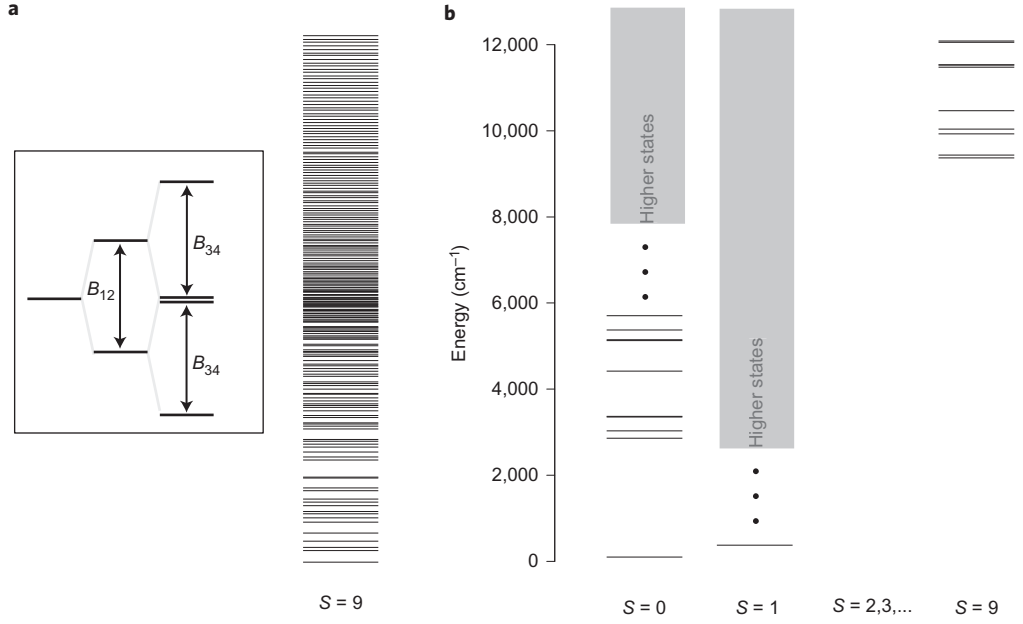

Figure 6 | Energy levels of the [4Fe–4S] cluster. The low-lying spectrum of the [4Fe–4S] cluster is unusually dense and is starkly different from the predictions of the simple HDE model. **a**, Isolated four low-lying states predicted (for each S) from the HDE model, compared to the qualitative *ab initio* density of states (shown for $S = 9$), **b**, Lowest-lying ten singlet ($S = 0$) and high spin ($S = 9$) states), as well as the ground-state triplet $S = 1$ state, showing the small energy scales and detailed structure of the spectrum.

but without slow spin-forbidden state crossings. Coupling between the spectrum and geometry allows for 'fine-tuning' of reactivity by the environment. [4Fe–4S] clusters thus appear to provide a conceptual bridge between molecular and surface catalytic reactivity. In the latter case, non-adiabatic processes on many potential energy surfaces are common, greatly modifying the timescales of electron and energy transfer[56].

Conclusions

To summarize, using the simplifying entanglement structure of physical many-particle quantum states, we have computed the individual ground- and excited-state energy levels of [2Fe–2S] and [4Fe–4S] clusters without model assumptions. Direct access to these energy levels has not previously been possible either through experiment or theory. Our calculations have allowed us to critically examine the validity of the consensus phenomenological models that have so far been the only way to understand FeS chemistry. In both the [2Fe–2S] dimer and the [4Fe–4S] cluster, we find that earlier understanding based on the canonical Heisenberg double exchange model underestimates the number of low-lying states by one to two orders of magnitude. These low-lying states arise from multi-orbital double-exchange processes. The new level spectrum we reveal has important implications for reactivity, as the density and accessibility of the low-lying states argues for the importance of multiple electronic states and non-adiabaticity in reactions. The theoretical techniques described here are potentially applicable to biological systems of even greater complexity, including the M- and P-clusters of nitrogenase[57,58]. More broadly, our work demonstrates new possibilities for realizing spectroscopy in complex systems by directly computing entangled electronic structure from many-particle quantum mechanics, without the need for *a priori* model assumptions.

Methods

All our DMRG calculations employed the Block code. Density functional calculations to obtain the initial geometries were carried out using the ORCA package. For DMRG calculations on the [2Fe–2S] clusters we used a full valence CAS (all Fe 3*d* and S 3*p* orbitals), and further included the Fe 4*s* and 4*d* shells to account for additional dynamic correlation effects. In the oxidized cluster, this corresponds to a 30-electron, 32-orbital active space. Even though the formal Hilbert space dimension is greater than 1×10^{17}, our calculations are enabled by the presence of some special entanglement structure in the states. In the [2Fe–2S] clusters we estimate that the electronic relative energies are converged to better than 0.1 kcal mol^{-1} (~35 cm^{-1}) of the exact active space results. For the [4Fe–4S] clusters we employed an active space with all Fe 3*d* and S 3*p* orbitals. These calculations were more expensive than the dimer calculations, so the DMRG energy differences between the singlet and triplet states are converged to only ~0.5–1 kcal mol^{-1}. These estimated errors refer to the errors from the corresponding CAS result. Dynamical correlation may lead to further small changes, as discussed in Supplementary Section 1.2. The higher singlet and high-spin states in Fig. 6 were calculated to lower accuracy than the ground singlet and triplet states, but are qualitatively correct. The multiplet states were computed explicitly without assuming any mutual interrelationship, in contrast to BS-DFT techniques, which only obtain the high-spin state and a weighted average of the multiplet energies, relying on model assumptions to deduce the individual levels[28]. All our computed wavefunctions exactly preserve spin (S^2) symmetry, due to the use of an SU(2) invariant DMRG code developed in our laboratory[40]. A full discussion of all the active spaces, geometry and examination of the DMRG convergence is presented in Supplementary Sections 1.1, 1.2, 2.1 and 2.2. For the spin correlation functions, S_1 and S_2 are defined from local Fe spin operators, and $\langle S_1 \cdot S_2 \rangle$ is the *ab initio* expectation value. These operators are defined in Supplementary equations (1) and (2).

Received 2 December 2013; accepted 24 July 2014; published online 31 August 2014

References

1. Beinert, H., Holm, R. H. & Münck, E. Iron–sulfur clusters: nature's modular, multipurpose structures. *Science* **277,** 653–659 (1997).
2. Johnson, D. C., Dean, D. R., Smith, A. D. & Johnson, M. K. Structure, function, and formation of biological iron–sulfur clusters. *Annu. Rev. Biochem.* **74,** 247–281 (2005).
3. Noodleman, L., Peng, C. Y., Case, D. A. & Mouesca, J. M. Orbital interactions, electron delocalization and spin coupling in iron–sulfur clusters. *Coord. Chem. Rev.* **144,** 199–244 (1995).
4. Zener, C. Interaction between the *d*-shells in the transition metals. II. Ferromagnetic compounds of manganese with perovskite structure. *Phys. Rev.* **82,** 403–405 (1951).
5. Anderson, P. W. & Hasegawa, H. Considerations on double exchange. *Phys. Rev.* **100,** 675–681 (1955).
6. Girerd, J-J. Electron transfer between magnetic ions in mixed valence binuclear systems. *J. Chem. Phys.* **79,** 1766–1775 (1983).
7. Noodleman, L. & Baerends, E. J. Electronic structure, magnetic properties, ESR, and optical spectra for 2-iron ferredoxin models by LCAO-Xα valence bond theory. *J. Am. Chem. Soc.* **106,** 2316–2327 (1984).
8. Noodleman, L. & Davidson, E. R. Ligand spin polarization and antiferromagnetic coupling in transition metal dimers. *Chem. Phys.* **109,** 131–143 (1986).
9. Papaefthymiou, V., Girerd, J. J., Moura, I., Moura, J. J. G. & Münck, E. Moessbauer study of *D. gigas* ferredoxin II and spin-coupling model for Fe_3S_4 cluster with valence delocalization. *J. Am. Chem. Soc.* **109,** 4703–4710 (1987).
10. Blondin, G. & Girerd, J. J. Interplay of electron exchange and electron transfer in metal polynuclear complexes in proteins or chemical models. *Chem. Rev.* **90,** 1359–1376 (1990).
11. Borshch, S. A., Kotov, I. N. & Bersuker, I. B. A vibronic model for exchange-coupled mixed-valence dimers. *Chem. Phys. Lett.* **111,** 264–270 (1984).
12. Labeguerie, P. *et al.* Is it possible to determine rigorous magnetic Hamiltonians in spin $s = 1$ systems from density functional theory calculations? *J. Chem. Phys.* **129,** 154110 (2008).
13. Gibson, J. F., Hall, D. O., Thornley, J. H. & Whatley, F. R. The iron complex in spinach ferredoxin. *Proc. Natl Acad. Sci. USA* **56,** 987–990 (1966).
14. Brintzinger, H., Palmer, G. & Sands, R. H. On the ligand field of iron in ferredoxin from spinach chloroplasts and related nonheme iron enzymes. *Proc. Natl Acad. Sci. USA* **55,** 397–404 (1966).
15. Rius, G. & Lamotte, B. Single-crystal ENDOR study of an ^{57}Fe-enriched iron–sulfur $[Fe_4S_4]^{3+}$ cluster. *J. Am. Chem. Soc.* **111,** 2464–2469 (1989).
16. Mouesca, J. M., Lamotte, B. & Rius, G. Comparison between spin population distributions in two different $[Fe_4S_4]^{3+}$ clusters by proton ENDOR in single crystals of a synthetic model compound. *J. Inorg. Biochem.* **43,** 251–270 (1991).
17. Bertini, I., Briganti, F., Luchinat, C., Scozzafava, A. & Sola, M. Proton NMR spectroscopy and the electronic structure of the high potential iron–sulfur protein from *Chromatium vinosum*. *J. Am. Chem. Soc.* **113,** 1237–1245 (1991).
18. Banci, L. *et al.* Proton NMR spectra of oxidized high-potential iron–sulfur protein (HiPIP) from *Rhodocyclus gelatinosus*. A model for oxidized HiPIPs. *Inorg. Chem.* **30,** 4517–4524 (1991).
19. Papaefthymiou, V., Millar, M. M. & Muenck, E. Moessbauer and EPR studies of a synthetic analog for the iron–sulfur Fe_4S_4 core of oxidized and reduced high-potential iron proteins. *Inorg. Chem.* **25,** 3010–3014 (1986).
20. Kappl, R., Ebelshäuser, M., Hannemann, F., Bernhardt, R. & Hüttermann, J. Probing electronic and structural properties of the reduced [2Fe–2S] cluster by orientation-selective ^{1}H ENDOR spectroscopy: adrenodoxin versus Rieske iron–sulfur protein. *Appl. Magn. Reson.* **30,** 427–459 (2006).
21. Maurice, R., Guihery, N., Bastardis, R. & de Graaf, C. Rigorous extraction of the anisotropic multispin Hamiltonian in bimetallic complexes from the exact electronic Hamiltonian. *J. Chem. Theor. Comput.* **6,** 55–65 (2009).
22. Noodleman, L., Norman, J. G., Osborne, J. H., Aizman, A. & Case, D. A. Models for ferredoxins: electronic structures of iron–sulfur clusters with one, two, and four iron atoms. *J. Am. Chem. Soc.* **107,** 3418–3426 (1985).
23. Mouesca, J-M., Chen, J. L., Noodleman, L., Bashford, D. & Case, D. A. Density functional/Poisson–Boltzmann calculations of redox potentials for iron–sulfur clusters. *J. Am. Chem. Soc.* **116,** 11898–11914 (1994).
24. Shoji, M. *et al.* Theory of chemical bonds in metalloenzymes III: full geometry optimization and vibration analysis of ferredoxin-type [2Fe–2S] cluster. *Int. J. Quantum Chem.* **107,** 116–133 (2007).
25. Noodleman, L. Valence bond description of antiferromagnetic coupling in transition metal dimers. *J. Chem. Phys.* **74,** 5737–5743 (1981).
26. Yamaguchi, K., Fueno, T., Ueyama, N., Akira, N. & Masaaki, O. Antiferromagnetic spin couplings between iron ions in ironsulfur clusters. a localized picture by the spin vector model. *Chem. Phys. Lett.* **164,** 210–216 (1989).
27. Yamaguchi, K., Fueno, T., Ozaki, M., Ueyama, N. & Nakamura, A. A general spin-orbital (GSO) description of antiferromagnetic spin couplings between four irons in iron–sulfur clusters. *Chem. Phys. Lett.* **168,** 56–62 (1990).
28. Neese, F. Prediction of molecular properties and molecular spectroscopy with density functional theory: from fundamental theory to exchange-coupling. *Coord. Chem. Rev.* **253,** 526–563 (2009).

29. Miralles, J., Daudey, J-P. & Caballol, R. Variational calculation of small energy differences. The singlet–triplet gap in $[Cu_2Cl_6]_2$. *Chem. Phys. Lett.* **198,** 555–562 (1992).
30. Miralles, J., Castell, O., Caballol, R. & Malrieu, J-P. Specific CI calculation of energy differences: transition energies and bond energies. *Chem. Phys.* **172,** 33–43 (1993).
31. Castell, O. & Caballol, R. *Ab-initio* configuration interaction calculation of the exchange coupling constant in hydroxo doubly bridged Cr(III) dimers. *Inorg. Chem.* **38,** 668–673 (1999).
32. Cabrero, J., Ben Amor, N., de Graaf, C., Illas, F. & Caballol, R. *Ab-initio* study of the exchange coupling in oxalato-bridged Cu(II) dinuclear complexes. *J. Phys. Chem. A* **104,** 9983–9989 (2000).
33. Hübner, O. & Sauer, J. The electronic states of $Fe_2S_2^{-/0/+/2+}$. *J. Chem. Phys.* **116,** 617–628 (2002).
34. Hastings, M. B. Entropy and entanglement in quantum ground states. *Phys. Rev. B* **76,** 35114 (2007).
35. Verstraete, F., Murg, V. & Cirac, J. I. Matrix product states, projected entangled pair states, and variational renormalization group methods for quantum spin systems. *Adv. Phys.* **57,** 143–224 (2008).
36. White, S. R. Density matrix formulation for quantum renormalization groups. *Phys. Rev. Lett.* **69,** 2863 (1992).
37. White, S. R. & Martin, R. L. *Ab initio* quantum chemistry using the density matrix renormalization group. *J. Chem. Phys.* **110,** 4127–4130 (1999).
38. Chan, G. K-L. & Sharma, S. The density matrix renormalization group in quantum chemistry. *Annu. Rev. Phys. Chem.* **62,** 465–481 (2011).
39. Kurashige, Y., Chan, G. K-L. & Yanai, T. Entangled quantum electronic wavefunctions of the Mn_4CaO_5 cluster in photosystem II. *Nature Chem.* **5,** 660–666 (2013).
40. Sharma, S. & Chan, G. K-L. Spin-adapted density matrix renormalization group algorithms for quantum chemistry. *J. Chem. Phys.* **136,** 124121 (2012).
41. Chan, G. K. L. & Head-Gordon, M. Highly correlated calculations with a polynomial cost algorithm: a study of the density matrix renormalization group. *J. Chem. Phys.* **116,** 4462–4476 (2002).
42. Zgid, D. & Nooijen, M. On the spin and symmetry adaptation of the density matrix renormalization group method. *J. Chem. Phys.* **128,** 014107 (2008).
43. Moritz, G., Hess, B. A. & Reiher, M. Convergence behavior of the density-matrix renormalization group algorithm for optimized orbital orderings. *J. Chem. Phys.* **122,** 024107 (2005).
44. Kurashige, Y. & Yanai, T. High-performance *ab initio* density matrix renormalization group method: applicability to large-scale multireference problems for metal compounds. *J. Chem. Phys.* **130,** 234114 (2009).
45. Legeza, Ö., Röder, J. & Hess, B. A. QC-DMRG study of the ionic-neutral curve crossing of LiF. *Mol. Phys.* **101,** 2019–2028 (2003).
46. Marti, K. H., Ondik, I. M., Mortise, G. & Reiher, M. Density matrix renormalization group calculations on relative energies of transition metal complexes and clusters. *J. Chem. Phys.* **128,** 014104 (2008).
47. Mayerle, J. J., Denmark, S. E., DePamphilis, B. V., Ibers, J. A. & Holm, R. H. Synthetic analogs of the active sites of iron–sulfur proteins. XI. Synthesis and properties of complexes containing the iron sulfide Fe_2S_2 core and the structures of bis[*o*-xylyl-α,α'-dithiolato-μ-sulfido-ferrate(III)] and bis[*p*-tolylthiolato-μ-sulfido-ferrate(III)] dianions. *J. Am. Chem. Soc.* **97,** 1032–1045 (1975).
48. Orme-Johnson, W. H. Iron–sulfur proteins: structure and function. *Annu. Rev. Biochem.* **42,** 159–204 (1973).
49. Venkateswara Rao, P. & Holm, R. H. Synthetic analogues of the active sites of iron sulfur proteins. *Chem. Rev.* **104,** 527–560 (2003).
50. Noodleman, L., Case, D., Mouesca, J-M. & Lamotte, B. Valence electron delocalization in polynuclear iron–sulfur clusters. *J. Biol. Inorg. Chem.* **1,** 177–182 (1996).
51. Gillum, W. O., Frankel, R. B., Foner, S. & Holm, R. H. Synthetic analogues of the active sites of iron–sulfur proteins. XIII. Further electronic structural relationships between the analogues $[Fe_2S_2(SR)_4]^{2-}$ and the active sites of oxidized 2Fe–2S* proteins. *Inorg. Chem.* **15,** 1095–1100 (1976).
52. Noodleman, L. & Case, D. A. Density-functional theory of spin polarization and spin coupling in iron–sulfur clusters. *Adv. Inorg. Chem* **38,** 423–470 (1992).
53. Averill, B. A., Herskovitz, T., Holm, R. H. & Ibers, J. A. Synthetic analogs of the active sites of iron–sulfur proteins. II. Synthesis and structure of the tetra [mercapto-μ3-sulfido-iron] clusters, $[Fe_4S_4(SR)_4]^{2-}$. *J. Am. Chem. Soc.* **95,** 3523–3534 (1973).
54. Noodleman, L., Lovell, T., Liu, T., Himo, F. & Torres, R. A. Insights into properties and energetics of iron–sulfur proteins from simple clusters to nitrogenase. *Curr. Opin. Chem. Biol.* **6,** 259–273 (2002).
55. Shaik, S., Kumar, D., de Visser, S. P., Altun, A. & Thiel, W. Theoretical perspective on the structure and mechanism of cytochrome P450 enzymes. *Chem. Rev.* **105,** 2279–2328 (2005).
56. Wodtke, A. M., Tully, J. C. & Auerbach, D. J. Electronically non-adiabatic interactions of molecules at metal surfaces: can we trust the Born–Oppenheimer approximation for surface chemistry? *Int. Rev. Phys. Chem.* **23,** 513–539 (2004).
57. Lancaster, K. M. *et al.* X-ray emission spectroscopy evidences a central carbon in the nitrogenase iron–molybdenum cofactor. *Science* **334,** 974–977 (2011).
58. Spatzal, T. *et al.* Evidence for interstitial carbon in nitrogenase FeMo cofactor. *Science* **334,** 940 (2011).

Acknowledgements

Work performed by S.S. and G.K.C. was supported by the US National Science Foundation (CHE-1265277) using software developed with the support of OCI-1265278. F.N. and K.S. acknowledge financial support from the Max Planck Society, the University of Bonn and the SFB 813 'Chemistry at Spin Centers'.

Author contributions

S.S. performed the DMRG calculations, analysed the results and contributed to writing the manuscript. F.N. contributed to writing the manuscript. K.S. performed geometry optimization for the [4Fe–4S] model cluster. G.K.C. wrote the manuscript and contributed to the calculations and analysis of the results. All authors discussed the results and commented on the manuscript.

Additional information

Supplementary information is available in the online version of the paper. Reprints and permissions information is available online at www.nature.com/reprints. Correspondence and requests for materials should be addressed to G.K.L.C.

Competing financial interests

The authors declare no competing financial interests.

nature chemistry

SUPPLEMENTARY INFORMATION

DOI: 10.1038/NCHEM.2041

Low-energy spectrum of iron-sulfur clusters directly from many-particle quantum mechanics

Sandeep Sharma, Kantharuban Sivalingam, Frank Neese, Garnet Kin-Lic Chan

Contents

1 [2Fe-2S] complexes

1.1 Geometry and orbitals

We used a [2Fe-2S] dimer obtained from the complex of Mayerle *et al* [1] by substituting the four terminal toluene groups with methyl groups. For the $[Fe_2S_2(SCH_3)_4]^{2-}$ complex, the ge-

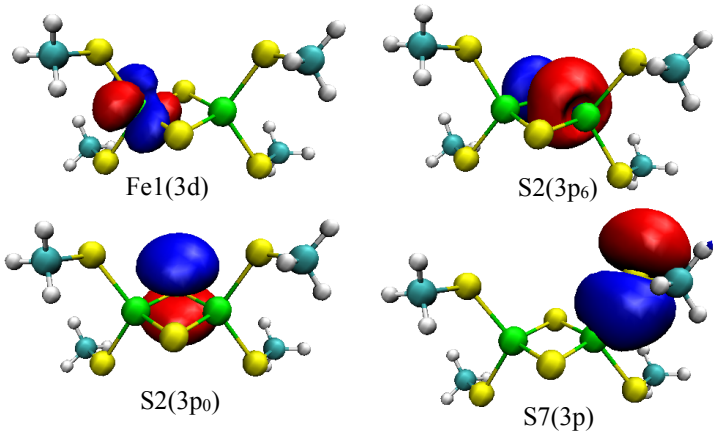

Supplementary Figure 1: Orbitals in the active space of the [2Fe-2S] dimers.

ometry was derived from the experimental structure reported in [1], as shown in Supplementary Table 1. For the $[Fe_2S_2(SCH_3)_4]^{3-}$ complex, we considered two geometries: (i) the geometry in Supplementary Table 1 (the same geometry as the $[Fe_2S_2(SCH_3)_4]^{2-}$ complex), and (ii) a relaxed geometry, shown in Supplementary Table 2. The relaxed geometry was obtained from a broken-symmetry DFT calculation on the S_z=1/2 state, using the BP86 functional and a split-valence with polarization (SVP) basis set [2] (denoted BP86/SVP) as implemented in Orca[3]. As seen from the table, in the relaxed geometry the dimer becomes slightly asymmetric, with the bridging S atoms attracted towards one of the Fe atoms.

To generate the active space for the DMRG calculations, we performed an unrestricted DFT BP86/SVP calculation for the high spin (S_z=5) state. The alpha occupied and unoccupied orbitals were then separately localized ("split-localized") [4] using the Pipek-Mezey algorithm [5]. From the localized orbitals, iron 3d, 4s, 4d and sulfur 3p orbitals were identified by visual inspection. Some of these orbitals are shown in Supplementary Figure 1.

Supplementary Table 1: Coordinates (in Å) of the $[Fe_2S_2(SCH_3)_4]^{2-}$ and unrelaxed $[Fe_2S_2(SCH_3)_4]^{3-}$ model complexes.

		x	y	z
1	Fe	5.22	1.05	-7.95
2	S	3.86	-0.28	-9.06
3	S	5.00	0.95	-5.66
4	S	4.77	3.18	-8.74
5	S	7.23	0.28	-8.38
6	Fe	5.88	-1.05	-9.49
7	S	6.10	-0.95	-11.79
8	S	6.33	-3.18	-8.71
9	C	6.00	4.34	-8.17
10	H	6.46	4.81	-9.01
11	H	5.53	5.08	-7.55
12	H	6.74	3.82	-7.60
13	C	3.33	1.31	-5.18
14	H	2.71	0.46	-5.37
15	H	3.30	1.54	-4.13
16	H	2.97	2.15	-5.73
17	C	5.10	-4.34	-9.28
18	H	5.56	-5.05	-9.93
19	H	4.67	-4.84	-8.44
20	H	4.34	-3.81	-9.81
21	C	7.77	-1.31	-12.27
22	H	7.84	-1.35	-13.34
23	H	8.42	-0.54	-11.90
24	H	8.06	-2.25	-11.86

Supplementary Table 2: Coordinates (in Å) of the relaxed $[Fe_2S_2(SCH_3)_4]^{3-}$ model complex.

		x	y	z
1	Fe	5.48	1.15	-8.03
2	S	4.05	-0.61	-8.75
3	S	5.47	1.25	-5.58
4	S	4.63	3.28	-8.77
5	S	7.49	0.42	-9.04
6	Fe	6.04	-1.22	-9.63
7	S	5.75	-1.50	-12.05
8	S	6.86	-3.41	-8.86
9	C	5.51	4.45	-7.51
10	H	6.49	4.83	-7.92
11	H	4.87	5.33	-7.25
12	H	5.72	3.84	-6.59
13	C	3.60	1.70	-5.54
14	H	3.01	0.80	-5.82
15	H	3.28	2.06	-4.52
16	H	3.42	2.48	-6.31
17	C	5.21	-4.22	-9.46
18	H	5.10	-4.01	-10.55
19	H	5.21	-5.32	-9.26
20	H	4.37	-3.72	-8.93
21	C	7.63	-1.85	-12.24
22	H	7.90	-2.06	-13.31
23	H	8.20	-0.96	-11.86
24	H	7.89	-2.72	-11.59

1.2 DMRG calculations

1.2.1 Active spaces

Four types of active space DMRG calculations (labelled (1)-(4)) were performed on the $[Fe_2S_2(SCH_3)_4]^{2-}$ complex to assess the effect of active space choice. For the $[Fe_2S_2(SCH_3)_4]^{3-}$ complex, we used only active spaces (1) and (2), following the analysis in section 1.2.3.

All DMRG calculations were spin-adapted, using the BLOCK code as described in Ref. [6]. Thus all states obtained are eigenfunctions of S_z and S^2, and M refers to the number of spin-adapted renormalized states (the tensor link dimension in the one-dimensional tensor network underlying the DMRG) which corresponds to effectively twice the number of non-spin-adapted renormalized states in a standard DMRG calculation [6]. The 4 types of DMRG calculations were:

1. DMRG-CI on a (30e, 20o) active space, with a maximum of M=3500 renormalized states. The 20 orbitals included Fe 3d, bridging S 3p, and one 3p orbital per terminal ligand S atom. This corresponds to a minimal full valence active space. For rapid convergence of the DMRG energy, the orbitals were ordered as follows: S4(3p), S3(3p), Fe1(3d), Fe1(3d), Fe1(3d), Fe1(3d), Fe1(3d), S2($3p_1$), S5($3p_1$), S2($3p_0$), S5($3p_0$), S2($3p_6$), S5($3p_6$), Fe6(3d), Fe6(3d), Fe6(3d), Fe6(3d), Fe6(3d), S7(3p), S8(3p), where the atom labels correspond to the labels in Supplementary Tables 1 and 2, and Figure 1, and the subscript on S 3p orbitals is the index of the atom they are pointing towards, with the exception that the subscript 0 means that it is pointing in the up-down direction as shown in Figure 1.

2. DMRG-CI on a (30e, 32o) active space, with a maximum of M=4500 renormalized states. The 30 orbitals include Fe 4d and Fe 4s orbitals in addition to the 20 described in active space (1). The Fe 4d and 4s orbitals are expected to account for the principal dynamic and orbital relaxation contributions to the energy (i.e. double-shell correlation [7]). The

orbitals were ordered as for the 20 orbital active space, with additional Fe 4s and Fe 4d orbitals placed in that order immediately following the 3d orbitals of the same Fe atom.

3. DMRG-SCF on the (30e, 20o) active space (cf. active space(1)). The active space orbitals were optimized using a self-consistent cycle. The DMRG calculations in the SCF optimization used M=2500 states. Subsequently a final calculation with M=3500 states, using the fixed optimized orbitals, was performed. The same ordering as in active space (1) was used.

4. DMRG-SCF on the (30e, 32o) active space (cf. active space (2)). Again, the DMRG calculations in the SCF optimization were performed with M=2500. Subsequently a final calculation with M=4500 states, using the fixed optimized orbitals, was performed. The same ordering as in active space (2) was used.

1.2.2 Energy convergence

The DMRG energies and discarded weights at different values of M can be used to extrapolate the energy to the $M = \infty$ (FCI) result, which corresponds to zero discarded weight. This also provides error estimates for the DMRG energy [8]. Extrapolations for state-specific DMRG-CI (active space 2) calculations are shown in Supplementary Table 3 and Supplementary Figure 2. We find that the extrapolated (30e, 32o) singlet and triplet relative energies are converged to within 0.1 mE_h of the FCI energy.

For the [2Fe-2S] spectrum calculations, we computed the lowest 10 states in each spin-sector using a state-averaged DMRG calculation. Although the energies are not as well converged as for the state-specific calculations, the residual errors do not qualitatively affect the spectrum or the conclusions of our analysis.

Supplementary Table 3: DMRG energy in E_h versus the discarded weight of the singlet and triplet states of the $[Fe_2S_2(SCH_3)_4]^{-2}$ cluster (active space (2), (30e, 32o)).

	Singlet		Triplet	
M	Discarded weight	Energy	Discarded weight	Energy
1500	2.45×10^{-5}	-5,104.138933	2.54×10^{-5}	-5,104.135801
2500	1.14×10^{-5}	-5,104.139978	1.23×10^{-5}	-5,104.137651
3500	5.63×10^{-6}	-5,104.140297	8.54×10^{-6}	-5,104.138315
4500	3.60×10^{-6}	-5,104.140426	6.03×10^{-6}	-5,104.138616
∞		-5,104.140718		-5,104.139510

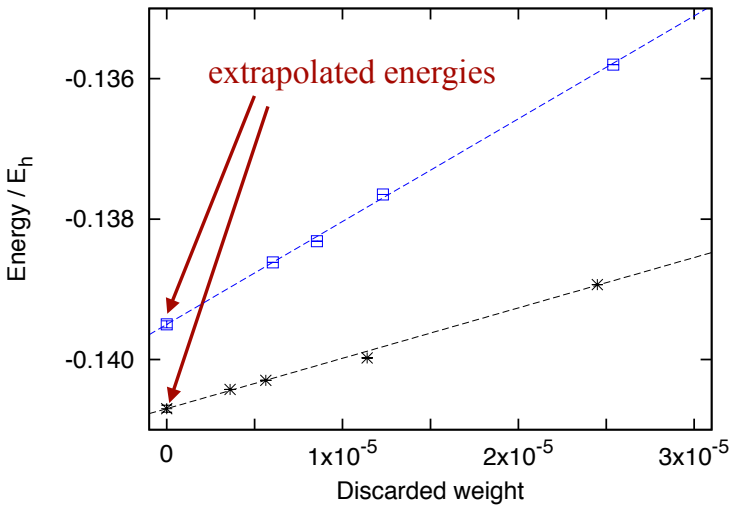

Supplementary Figure 2: DMRG energy (E+5104.0) in E_h of the singlet and triplet states versus the discarded weight of the $[Fe_2S_2(SCH_3)_4]^{-2}$ cluster (active space (2), (30e, 32o). The black crosses and the blue dots are respectively the DMRG singlet and triplet state energies and the corresponding lines are the best fit straight lines which are extrapolated to zero discarded weight to obtain an estimated FCI energy.

Supplementary Table 4: The singlet-triplet gap of the $[Fe_2S_2(SCH_3)_4]^{2-}$ complex obtained in active spaces (1)-(4).

Method	Active Space	Gap/mE_h
DMRG-CI	(30e, 20o)	1.5
DMRG-CI	(30e, 32o)	2.1
DMRG-SCF	(30e, 20o)	1.2
DMRG-SCF	(30e, 32o)	2.0

1.2.3 Assessment of active space

From the singlet-triplet gap in the active spaces (1)-(4), shown in Supplementary Table 4, we can assess the effect of the active space choice on the computed energy levels. We first observe that all 4 active spaces agree closely; even the minimal valence active space yields a reasonable gap. This is because the principle exchange pathway leading to the singlet-triplet gap is via the bridging S 3p ligand orbitals, which are included in the minimal active space. The effect of double-shell correlation in the larger active spaces is to increase the gap by less than 1.0mE_h, while the effect of orbital optimization is very small (0.1mE_h in the larger active space). We take active space (2) (double shell correlation but no orbital optimization) as a practical compromise between accuracy and efficiency.

1.3 Local charge and spin

To identify the distribution of electrons, we have computed local populations on the atoms. For atom A, the local population N_A is

$$N_A = \sum_{i \in A} n_i \tag{1}$$

where n_i is the number operator of localized orbital i on the A.

Further, since our states are eigenstates of S^2, there is no spin-density in the singlet states. Thus, we have computed local spins and spin-correlation functions to characterize the electronic

structure. The spin-correlation function between atoms A and B, $\langle S_A \cdot S_B \rangle$, is defined as [9, 10, 11]

$$\begin{aligned} S_A \cdot S_B &= \sum_{\alpha} S_A^{\alpha} S_B^{\alpha} \\ S_A^{\alpha} &= \sum_{i \in A} s_i^{\alpha} \end{aligned} \tag{2}$$

where $\alpha \in \{x, y, z\}$. The local total spin on atom A is defined as $\langle S_A \cdot S_A \rangle$.

Supplementary Tables 6-9 show the relative energies, local populations, spins, and spin-correlation functions for the [2Fe-2S] complexes. All the relative energies reported in the tables are calculated using active space (2). For both geometries state averaged DMRG calculations are performed for the first 10 states with a largest M of 4500. In the case of unrelaxed geometries three sweeps with M=4500 were performed and then its value was reduced in steps of 1000 down to M=1500 to generate reliable extrapolated energies. We find that even though the extrapolation process improves the absolute energies, the energy differences reported in the tables are relatively unchanged. We expect to see the same trend for the relaxed geometries and thus forego the expensive extrapolation step to report the relative DMRG energies calculated with M=4500.

In Supplementary Table 6 and Supplementary Table 8 only the 3d, 4s and 4d orbitals of a Fe atom are included in the summations in Equations 1 and 2 to calculate the local electron density and electron spin; whereas in Supplementary Table 7 and Supplementary Table 9 the first 16 orbitals and second 16 orbitals (see orbital ordering in previous section for the orbitals) are included in the summations for first and the second Fe atoms respectively. The ideal Fe^{II} and Fe^{III} populations are 6 and 5 respectively, while the ideal S=2 and S=5/2 total spins are 6 and 8.75 respectively. We see that the observed local populations and total spins are increased and reduced respectively in the complexes due to the effect of quantum fluctuations, such as delocalization onto adjacent sulfur orbitals. We also see from the spin-correlation functions

Supplementary Table 5: The local population, total spin, and spin-correlation functions in the lowest spin states of the $[Fe_2S_2(SCH_3)_4]^{2-}$ complex, using active space (2). Note $\langle N_2 \rangle = \langle N_1 \rangle$ and $\langle S_2^2 \rangle = \langle S_1^2 \rangle$. One orbitals of the Fe

Dimer S	$\langle N_1 \rangle$	$\langle S_1^2 \rangle$	$\langle S_1 \cdot S_2 \rangle$
0	6.18	5.47	-4.92
1	6.17	5.47	-4.22
2	6.17	5.49	-2.84
3	6.17	5.51	-0.79
4	6.16	5.54	1.84
5	6.13	5.74	3.74

that the spins progressively move from being anti-aligned to aligned as the the total dimer spin is increased.

1.3.1 Asymmetry in the $[Fe_2S_2(SCH_3)_4]^{3-}$ complex

The relaxed geometry of the $[Fe_2S_2(SCH_3)_4]^{3-}$ complex is slightly asymmetric. The local populations and spins in Supplementary Table 8 and 9 show the effect of this asymmetry on the electronic structure. As observed in Supplementary Table 8 the asymmetry in the Fe atoms appears rather small, amounting to up to 0.05 electron units in the population, and 0.2 spin units in the local spin. But when we compare the local spins shown in Supplementary Table 9, the asymmetry is much larger with differences between the local spins as large as 2.4 in some cases. The difference in asymmetry between the two tables points to the fact that the asymmetry is largely due to the difference in the S 3p orbitals.

1.4 Model Hamiltonian for the $[Fe_2S_2(SCH_3)_4]^{3-}$ dimer

The energy levels of the HDE model for the $[Fe_2S_2(SCH_3)_4]^{3-}$ mixed valence complex, as derived by Noodleman and Baerends, are given by

$$E(S) = 2JS_1 \cdot S_2 \pm B(S + 1/2) \tag{3}$$

Supplementary Table 6: Unrelaxed geometry $[Fe_2S_2(SCH_3)_4]^{3-}$ energy (cm^{-1}), local population, total spin and spin-correlation functions for the lowest ten levels in each dimer total spin state, using active space (2).

State	1	2	3	4	5	6	7	8	9	10
S=1/2										
E	0	325	1132	2642	4264	4989	4905	5313	6448	7049
$\langle N_1 \rangle$	6.23	6.25	6.24	6.23	6.22	6.21	6.22	6.21	6.21	6.21
$\langle N_2 \rangle$	6.24	6.23	6.24	6.23	6.22	6.22	6.21	6.21	6.21	6.21
$\langle S_1 \rangle$	5.39	5.31	5.34	5.35	5.39	5.40	5.36	5.43	5.40	5.42
$\langle S_2 \rangle$	5.32	5.36	5.34	5.35	5.36	5.37	5.43	5.42	5.41	5.42
$\langle S_1 \cdot S_2 \rangle$	-4.74	-4.77	-4.81	-4.62	-4.84	-4.72	-4.83	-4.89	-4.78	-4.77
S=3/2										
E	136	527	1710	4264	4451	5030	5131	6073	7870	8581
$\langle N_1 \rangle$	6.22	6.24	6.24	6.22	6.21	6.21	6.21	6.22	6.21	6.20
$\langle N_2 \rangle$	6.23	6.24	6.23	6.22	6.22	6.21	6.21	6.21	6.21	6.20
$\langle S_1 \rangle$	5.42	5.35	5.34	5.37	5.40	5.42	5.43	5.38	5.42	5.43
$\langle S_2 \rangle$	5.39	5.36	5.36	5.37	5.40	5.42	5.43	5.41	5.42	5.43
$\langle S_1 \cdot S_2 \rangle$	-3.66	-3.77	-3.64	-3.38	-3.68	-3.79	-3.78	-3.47	-3.61	-3.59
S=5/2										
E	336	643	2871	4668	5300	5678	6248	7580	9459	10260
$\langle N_1 \rangle$	6.21	6.23	6.23	6.20	6.21	6.20	6.22	6.21	6.20	6.20
$\langle N_2 \rangle$	6.22	6.24	6.23	6.21	6.21	6.21	6.22	6.20	6.20	6.20
$\langle S_1 \rangle$	5.50	5.38	5.37	5.45	5.44	5.46	5.38	5.41	5.44	5.43
$\langle S_2 \rangle$	5.45	5.37	5.38	5.43	5.44	5.44	5.39	5.45	5.45	5.44
$\langle S_1 \cdot S_2 \rangle$	-1.89	-1.96	-1.77	-1.81	-1.91	-1.95	-1.33	-1.51	-1.68	-1.67
S=7/2										
E	669	1330	4675	5441	6358	7049	8989	9589	9913	10115
$\langle N_1 \rangle$	6.19	6.22	6.22	6.19	6.19	6.20	6.20	6.25	6.22	6.28
$\langle N_2 \rangle$	6.20	6.23	6.22	6.19	6.21	6.19	6.21	6.27	6.24	6.30
$\langle S_1 \rangle$	5.56	5.43	5.43	5.50	5.51	5.50	5.45	5.02	5.29	4.76
$\langle S_2 \rangle$	5.55	5.42	5.44	5.51	5.46	5.54	5.40	5.00	5.25	4.76
$\langle S_1 \cdot S_2 \rangle$	0.55	0.60	0.78	0.78	0.67	0.61	1.38	2.16	1.72	2.49
S=9/2										
E	1071	2943	7357	7403	8496	9209	13263	13699	14803	15073
$\langle N_1 \rangle$	6.18	6.21	6.16	6.20	6.19	6.17	6.17	6.17	6.17	6.22
$\langle N_2 \rangle$	6.19	6.21	6.16	6.20	6.18	6.17	6.17	6.17	6.17	6.22
$\langle S_1 \rangle$	5.63	5.57	5.68	5.59	5.60	5.64	5.65	5.65	5.64	5.53
$\langle S_2 \rangle$	5.62	5.56	5.67	5.58	5.62	5.65	5.66	5.65	5.64	5.53
$\langle S_1 \cdot S_2 \rangle$	3.62	3.58	3.67	3.60	3.62	3.65	3.66	3.65	3.65	3.56

Supplementary Table 7: Unrelaxed geometry $[Fe_2S_2(SCH_3)_4]^{3-}$ energy (cm^{-1}), local population, total spin and spin-correlation functions for the lowest ten levels in each dimer total spin state, using active space (2). The orbitals taken to

State	1	2	3	4	5	6	7	8	9	10
S=1/2										
E	0	325	1132	2642	4264	4989	4905	5313	6448	7049
$\langle N_1 \rangle$	15.48	15.50	15.49	15.49	15.49	15.48	15.52	15.49	15.50	15.49
$\langle N_2 \rangle$	15.52	15.50	15.51	15.51	15.51	15.52	15.48	15.51	15.50	15.51
$\langle S_1 \rangle$	5.87	5.63	5.77	5.64	5.84	5.78	5.62	5.84	5.74	5.76
$\langle S_2 \rangle$	5.61	5.84	5.76	5.68	5.63	5.59	5.95	5.83	5.79	5.78
$\langle S_1 \cdot S_2 \rangle$	-5.37	-5.36	-5.39	-5.28	-5.36	-5.31	-5.41	-5.46	-5.39	-5.40
S=3/2										
E	136	527	1710	4264	4451	5030	5131	6073	7870	8581
$\langle N_1 \rangle$	15.49	15.50	15.50	15.49	15.50	15.49	15.49	15.50	15.50	15.49
$\langle N_2 \rangle$	15.51	15.50	15.50	15.51	15.50	15.51	15.51	15.50	15.50	15.51
$\langle S_1 \rangle$	6.00	5.95	5.85	5.76	5.93	6.00	5.99	5.74	5.89	5.90
$\langle S_2 \rangle$	5.89	5.98	5.92	5.78	5.86	5.95	5.98	5.84	5.91	5.88
$\langle S_1 \cdot S_2 \rangle$	-4.07	-4.09	-4.01	-3.90	-4.02	-4.10	-4.11	-3.91	-4.03	-4.01
S=5/2										
E	336	643	2871	4668	5300	5678	6248	7580	9459	10260
$\langle N_1 \rangle$	15.49	15.49	15.50	15.50	15.49	15.49	15.49	15.50	15.50	15.49
$\langle N_2 \rangle$	15.51	15.51	15.50	15.50	15.51	15.51	15.51	15.50	15.50	15.51
$\langle S_1 \rangle$	6.35	6.27	6.13	6.24	6.24	6.32	5.91	5.95	6.11	6.12
$\langle S_2 \rangle$	6.22	6.25	6.17	6.18	6.26	6.16	5.94	6.10	6.16	6.13
$\langle S_1 \cdot S_2 \rangle$	-1.91	-1.89	-1.78	-1.84	-1.87	-1.87	-1.55	-1.65	-1.76	-1.75
S=7/2										
E	669	1330	4675	5441	6358	7049	8989	9589	9913	10115
$\langle N_1 \rangle$	15.49	15.49	15.50	15.50	15.48	15.50	15.48	15.46	15.46	15.54
$\langle N_2 \rangle$	15.51	15.51	15.50	15.50	15.52	15.50	15.52	15.54	15.54	15.46
$\langle S_1 \rangle$	6.76	6.67	6.55	6.56	6.70	6.62	6.31	5.59	5.98	5.46
$\langle S_2 \rangle$	6.78	6.69	6.61	6.67	6.62	6.76	6.19	5.65	5.97	5.21
$\langle S_1 \cdot S_2 \rangle$	1.10	1.19	1.30	1.26	1.22	1.19	1.63	2.26	1.90	2.54
S=9/2										
E	1071	2943	7357	7403	8496	9209	13263	13699	14803	15073
$\langle N_1 \rangle$	15.49	15.49	15.50	15.49	15.50	15.49	15.48	15.51	15.49	15.50
$\langle N_2 \rangle$	15.51	15.51	15.50	15.51	15.50	15.51	15.52	15.49	15.51	15.50
$\langle S_1 \rangle$	7.44	7.43	7.41	7.45	7.42	7.44	7.46	7.39	7.44	7.42
$\langle S_2 \rangle$	7.40	7.40	7.40	7.38	7.41	7.39	7.37	7.44	7.38	7.40
$\langle S_1 \cdot S_2 \rangle$	4.95	4.96	4.97	4.96	4.96	4.96	4.96	4.96	4.96	4.96

Supplementary Table 8: Relaxed geometry $[Fe_2S_2(SCH_3)_4]^{3-}$ energy (cm^{-1}), local population, total spin and spin-correlation functions for the lowest ten levels in each dimer total spin state, using active space (2).

State	1	2	3	4	5	6	7	8	9	10
S=1/2										
E	0	1218	2079	3790	4070	4314	4885	5731	6975	7644
$\langle N_1 \rangle$	6.26	6.24	6.16	6.18	6.21	6.21	6.20	6.17	6.17	6.17
$\langle N_2 \rangle$	6.14	6.16	6.28	6.25	6.16	6.16	6.16	6.23	6.22	6.22
$\langle S_1 \rangle$	5.32	5.37	5.67	5.63	5.45	5.42	5.48	5.62	5.65	5.64
$\langle S_2 \rangle$	5.73	5.67	5.18	5.26	5.68	5.67	5.65	5.33	5.34	5.31
$\langle S_1 \cdot S_2 \rangle$	-4.96	-5.01	-4.85	-4.78	-5.03	-5.04	-5.02	-4.86	-4.90	-4.89
S=3/2										
E	266	1211	2374	4197	4493	4694	4925	6460	7693	8342
$\langle N_1 \rangle$	6.24	6.23	6.17	6.20	6.19	6.18	6.19	6.17	6.17	6.24
$\langle N_2 \rangle$	6.15	6.17	6.26	6.18	6.19	6.21	6.16	6.22	6.21	6.28
$\langle S_1 \rangle$	5.37	5.42	5.64	5.50	5.53	5.57	5.49	5.61	5.63	5.37
$\langle S_2 \rangle$	5.72	5.63	5.28	5.61	5.51	5.44	5.67	5.39	5.39	4.93
$\langle S_1 \cdot S_2 \rangle$	-3.86	-3.97	-3.75	-3.90	-3.74	-3.67	-3.89	-3.61	-3.72	-2.71
S=5/2										
E	623	1323	2848	4619	4913	5200	5943	7536	8374	8715
$\langle N_1 \rangle$	6.23	6.22	6.18	6.18	6.18	6.19	6.18	6.17	6.24	6.18
$\langle N_2 \rangle$	6.15	6.18	6.22	6.20	6.17	6.16	6.23	6.21	6.28	6.21
$\langle S_1 \rangle$	5.44	5.47	5.59	5.57	5.55	5.52	5.60	5.62	5.34	5.61
$\langle S_2 \rangle$	5.70	5.62	5.44	5.52	5.61	5.67	5.38	5.43	4.98	5.41
$\langle S_1 \cdot S_2 \rangle$	-2.03	-2.16	-1.96	-1.98	-2.04	-2.03	-1.43	-1.59	-0.24	-1.76
S=7/2										
E	786	1405	3375	5173	5368	5696	7528	8254	8863	9149
$\langle N_1 \rangle$	6.21	6.21	6.20	6.17	6.17	6.18	6.17	6.24	6.17	6.24
$\langle N_2 \rangle$	6.15	6.18	6.18	6.17	6.21	6.16	6.22	6.27	6.20	6.27
$\langle S_1 \rangle$	5.52	5.51	5.55	5.60	5.63	5.57	5.61	5.33	5.62	5.33
$\langle S_2 \rangle$	5.70	5.62	5.61	5.62	5.52	5.67	5.42	5.03	5.47	5.06
$\langle S_1 \cdot S_2 \rangle$	0.50	0.39	0.53	0.60	0.60	0.52	1.33	3.07	1.18	2.98
S=9/2										
E	984	1839	4254	5941	6458	6873	10136	11196	11377	12487
$\langle N_1 \rangle$	6.19	6.20	6.20	6.16	6.17	6.15	6.15	6.15	6.18	6.16
$\langle N_2 \rangle$	6.16	6.18	6.15	6.14	6.17	6.21	6.20	6.19	6.21	6.19
$\langle S_1 \rangle$	5.60	5.57	5.56	5.68	5.66	5.71	5.70	5.70	5.64	5.69
$\langle S_2 \rangle$	5.72	5.66	5.73	5.74	5.67	5.55	5.58	5.60	5.56	5.59
$\langle S_1 \cdot S_2 \rangle$	3.66	3.63	3.66	3.71	3.68	3.65	3.66	3.67	3.63	3.66

Supplementary Table 9: Relaxed geometry $[Fe_2S_2(SCH_3)_4]^{3-}$ energy (cm^{-1}), local population, total spin and spin-correlation functions for the lowest ten levels in each dimer total spin state, using active space (2).

State	1	2	3	4	5	6	7	8	9	10
S=1/2										
E	0	1218	2079	3790	4070	4314	4885	5731	6975	7644
$\langle N_1 \rangle$	15.62	15.59	15.37	15.39	15.61	15.61	15.58	15.41	15.37	15.38
$\langle N_2 \rangle$	15.38	15.41	15.63	15.61	15.39	15.39	15.42	15.59	15.63	15.62
$\langle S_1 \rangle$	5.05	5.20	7.31	7.11	5.24	5.26	5.30	6.89	7.28	7.23
$\langle S_2 \rangle$	7.42	7.25	5.04	5.13	7.30	7.27	7.02	5.31	5.11	5.02
$\langle S_1 \cdot S_2 \rangle$	-5.86	-5.85	-5.80	-5.74	-5.89	-5.89	-5.79	-5.72	-5.82	-5.75
S=3/2										
E	266	1211	2374	4197	4493	4694	4925	6460	7693	8342
$\langle N_1 \rangle$	15.61	15.56	15.40	15.57	15.53	15.46	15.58	15.43	15.40	15.30
$\langle N_2 \rangle$	15.39	15.44	15.60	15.43	15.47	15.54	15.42	15.57	15.60	15.70
$\langle S_1 \rangle$	5.38	5.70	7.11	5.79	5.95	6.57	5.55	6.80	7.09	6.21
$\langle S_2 \rangle$	7.38	7.10	5.51	6.96	6.43	6.05	7.07	5.53	5.47	5.11
$\langle S_1 \cdot S_2 \rangle$	-4.51	-4.53	-4.43	-4.50	-4.32	-4.43	-4.44	-4.29	-4.41	-3.78
S=5/2										
E	623	1323	2848	4619	4913	5200	5943	7536	8374	8715
$\langle N_1 \rangle$	15.60	15.55	15.45	15.51	15.54	15.59	15.42	15.43	15.29	15.41
$\langle N_2 \rangle$	15.40	15.45	15.55	15.49	15.46	15.41	15.58	15.57	15.71	15.59
$\langle S_1 \rangle$	5.90	6.19	6.83	6.45	6.15	5.85	6.72	6.88	5.55	7.01
$\langle S_2 \rangle$	7.33	7.10	6.25	6.65	6.91	7.19	5.79	5.71	5.27	5.83
$\langle S_1 \cdot S_2 \rangle$	-2.24	-2.27	-2.16	-2.18	-2.16	-2.15	-1.88	-1.92	-1.03	-2.05
S=7/2										
E	786	1405	3375	5173	5368	5696	7528	8254	8863	9149
$\langle N_1 \rangle$	15.58	15.54	15.51	15.53	15.48	15.57	15.43	15.28	15.42	15.39
$\langle N_2 \rangle$	15.42	15.46	15.49	15.47	15.52	15.43	15.57	15.72	15.58	15.61
$\langle S_1 \rangle$	6.53	6.69	6.76	6.68	6.92	6.50	6.66	5.01	7.10	5.29
$\langle S_2 \rangle$	7.37	7.23	7.00	7.06	6.69	7.26	6.17	5.46	5.90	5.23
$\langle S_1 \cdot S_2 \rangle$	0.92	0.92	0.99	1.00	1.07	1.00	1.46	2.64	1.38	2.61
S=9/2										
E	984	1839	4254	5941	6458	6873	10136	11196	11377	12487
$\langle N_1 \rangle$	15.56	15.54	15.57	15.55	15.54	15.42	15.48	15.29	15.37	15.44
$\langle N_2 \rangle$	15.44	15.46	15.43	15.45	15.46	15.58	15.52	15.71	15.63	15.56
$\langle S_1 \rangle$	7.23	7.28	7.20	7.25	7.27	7.60	7.45	7.95	7.74	7.56
$\langle S_2 \rangle$	7.55	7.50	7.57	7.53	7.51	7.18	7.33	6.83	7.03	7.21
$\langle S_1 \cdot S_2 \rangle$	4.98	4.99	4.99	4.98	4.99	4.98	4.99	4.98	4.99	4.99

As demonstrated in the main text, the HDE energy levels do not fit the *ab-initio* DMRG spectrum well because of the assumptions used to derive Eq. (3). Before deriving a more complete model that *is* compatible with the *ab-initio* spectrum, we briefly recall how Eq. (3) is obtained from Anderson's analysis of double exchange [12, 13, 14].

We first consider an oxidized complex with two ferric ions (with spins $S_1 = 5/2$, $S_2 = 5/2$) as a "base" system. The extra electron in the reduced dimer is added to this base system, where it hops between a pair of local orbitals on each of the ions. Denoting the creation (annihilation) operators for the local orbitals on the first (second) ions by $c_1^{(\dagger)}$, $c_2^{(\dagger)}$ respectively, and the spin of the electron as s_1, s_2 respectively, Anderson's analysis[12] leads to a Hamiltonian of the form

$$H = J(S_1 \cdot S_2 + S_1 \cdot s_2 + S_2 \cdot s_1) + \sum_{\sigma=\uparrow,\downarrow} \beta(c_{1\sigma}^\dagger c_{2\sigma} + c_{2\sigma}^\dagger c_{1\sigma}) \tag{4}$$

where the Hamiltonian is to be solved in the Hilbert space where the hopping electron is always anti-aligned with the spin of the ferric ion on which it is currently residing. The terms in H have the following meaning:

1. The first corresponds to Heisenberg exchange coupling between spins on the two ions (the "base" ferric spins and the extra spin of the hopping electron).

2. The second describes the effective hopping of the electron between the two ferric ions (the sum over σ is a summation over electron spin).

The eigenvalues of the Anderson Hamiltonian may be determined analytically to be the HDE energy levels in Eq. (3), where $B = \beta/(2S+1)$, $S = S_1 = S_2$.

As argued in the main text, the most commonly used version of the HDE model breaks down in the $[Fe_2S_2(SCH_3)_4]^{3-}$ dimer because it assumes that there is a *single* pair of d orbitals on the ferric ions that participates in the hopping process. This assumption is valid if the double exchange splitting $B(S+1/2)$ is much smaller than the ligand-field splitting Δ. However, this is

clearly not the case for Fe ions with tetrahedral coordination which is typically associated with weak ligand fields. Instead, all 5 pairs of d orbitals participate in the hopping at low energies.

We can extend Anderson's double exchange Hamiltonian to multi-orbital double exchange. We label each of the 5 local d orbitals by index i. This gives

$$H = \sum_{ij} J_{ij} s_{1i} \cdot s_{2j} + \sum_{i\sigma} \left[\beta_i (c^\dagger_{1i\sigma} c_{2i\sigma} + c^\dagger_{2i\sigma} c_{1i\sigma}) + \Delta_i (c^\dagger_{1i\sigma} c_{1i\sigma} + c^\dagger_{2i\sigma} c_{2i\sigma}) \right] \quad (5)$$

where we once again restrict ourselves to states where the hopping electron is strictly antiferromagnetically aligned to the base spins (the base spins are all ferromagnetically aligned). The additional Δ_i term gives the ligand field splitting of the orbitals. The above form has a very large number of parameters from the general exchange couplings J_{ij}. However, in the limiting case where all spins are aligned on each Fe atom (e.g. as in the oxidized dimer), then it is sufficient to consider an exchange term of the form $\sum_i J'_i s_{1i} \cdot s_{2i}$ since the interaction of any spin on a given Fe atom, with any spin on the other Fe atom is the same, i.e. $s_{11} \cdot s_{21} = s_{1i} \cdot s_{21}$ for all i, and $J_i = \sum_j J_{ij}$. Keeping this form for the reduced dimer, we arrive at an Anderson Hamiltonian

$$H = \sum_{i} J_{i} s_{1i} \cdot s_{2i} + \sum_{i\sigma} \left[\beta_i (c^\dagger_{1i\sigma} c_{2i\sigma} + c^\dagger_{2i\sigma} c_{1i\sigma}) + \Delta_i (c^\dagger_{1i\sigma} c_{1i\sigma} + c^\dagger_{2i\sigma} c_{2i\sigma}) \right] \quad (6)$$

which is the one used in the main text. Note that when solving for the eigenvalues of the Hamiltonian, we restrict each ion to have at most one additional electron (i.e. the lowest oxidation state is ferrous).

The above multi-orbital Hamiltonian does not admit an analytic solution. However, we can solve for its eigenvalues and eigenvectors numerically. We have written a code to do this which works with an arbitrary number of base spins and hopping electrons and which we use also with the [4Fe-4S] Hamiltonian discussed later. The code is made efficient by working in the basis where the hopping electron is strictly anti-ferromagnetically aligned to the base spins.

Supplementary Table 10: The best-fit parameters (cm^{-1}) of the extended Anderson's double exchange Hamiltonian given in Equation 6 used to fit the low-lying energy levels of the $[Fe_2S_2(SCH_3)_4]^{3-}$ dimer. Note that J_i and β_i do *not* correspond to the exchange and double exchange parameters in the standard HDE model and cannot be directly compared. Standard deviations (as estimated from the covariance matrix of the fit) given in brackets.

	J_i	β_i	Δ_i
1	2656 ($\pm$513)	3512 ($\pm$280)	
2	2743 ($\pm$682)	9679 ($\pm$294)	1536 ($\pm$271)
3	2151 ($\pm$518)	4653 ($\pm$296)	4433 ($\pm$196)
4	1756 ($\pm$675)	8472 ($\pm$294)	6167 ($\pm$268)
5	395 ($\pm$695)	6562 ($\pm$296)	6167 ($\pm$284)

The hopping matrix elements in this basis can be calculated using Clebsch-Gordan coefficients, similar to Anderson's original work [12]. The code can be downloaded with this paper.

A direct fit of the multi-orbital Hamiltonian to the DMRG *ab-initio* levels yields the parameters in Supplementary Table 10 and the levels in Supplementary Figure 3. As we can see the fit is very good; the r.m.s. error is only about 60 cm^{-1}. Further it is very robust: out of 12 random initial starting fits, all fits either converged to the same physical solution shown (to within the standard deviation in the parameters), or attempted to find unphysical solutions with negative parameters. Overall, this demonstrates that the multi-orbital Hamiltonian indeed captures the essential low-energy physics of the $[Fe_2S_2(SCH_3)_4]^{3-}$ complex. Note that the plots in Fig. 3 are for dimer spins S=1/2, 3/2, 5/2 only. This is because for the higher dimer spins, some of the excited states appear to have acquire d-d transition character, i.e. the Fe ions are not truly high spin. This can be seen, for example in states 8 and 10 for S=7/2 in Supplementary Table 6. Such states probably exist in the weak-shoulder region below 10000 cm^{-1} in the low-temperature absorption spectrum of ferredoxins [15], and cannot be described with the model Hamiltonians we are using.

As emphasized in the text, the multi-orbital Hamiltonian is *not* equivalent to the simple

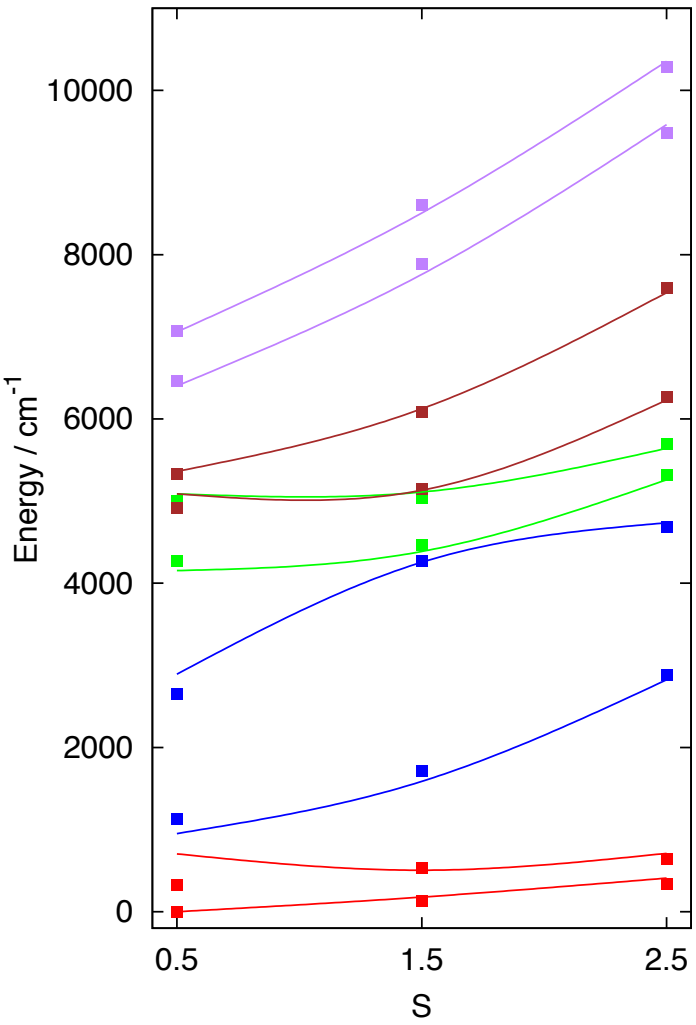

Supplementary Figure 3: Fit of first 10 states each with spins from S=1/2 to 5/2 using the multi-orbital Anderson model (see Equation 6).

multi-pair generalization of the HDE model. This would correspond to extending the HDE energy levels in Eq. (3) to 5 separate pairs of levels arising from each of the pair of d orbitals,

$$E_i(S) = \Delta_i + 2J_i S_1 \cdot S_2 \pm B_i(S_i + 1/2) \tag{7}$$

where the subscript i denotes the pair involved in the hopping. This multi-pair HDE model in fact has the same number of parameters as the multi-orbital Hamiltonian (6) itself. However, as seen in the Supplementary Figure 3 in the main text, the naive form does *not* fit the *ab-initio* DMRG results. Multi-orbital double exchange *cannot generally be viewed simply as the sum of individual orbital double-exchange processes*. In particular, this means that to be precise we should not characterize double exchange by an effective B parameter as in the HDE model, but rather by hopping integrals, β.

Further support for the multi-orbital nature of the double exchange is obtained from density difference plots, shown in Supplementary Figure 5. These plots are obtained as the difference density between different singlet states. If a single well-defined d orbital pair were to give rise to a pair of states, then we would expect the density difference to resemble a density associated with a particular d pair. However, we find that, aside from the lowest two pair of states (which appear to have some e_g parentage), the remaining density differences involve contributions from all sets of d orbital densities.

We now briefly discuss the effect of geometry relaxation on the $[Fe_2S_2(SCH_3)_4]^{3-}$ dimer energy levels. At the relaxed geometry, some localization of the charge occurs. The computed DMRG energy levels at the relaxed geometry are shown in Fig. 4. We find that our main observations are unchanged: there is little separation between the lowest two and higher energy levels, and the gap between the lowest two levels does not monotonically increase as required by the HDE model. We have not computed further relaxation effects from solvent and vibronic coupling, but it is clear from the above that our conclusions about the multi-orbital nature of

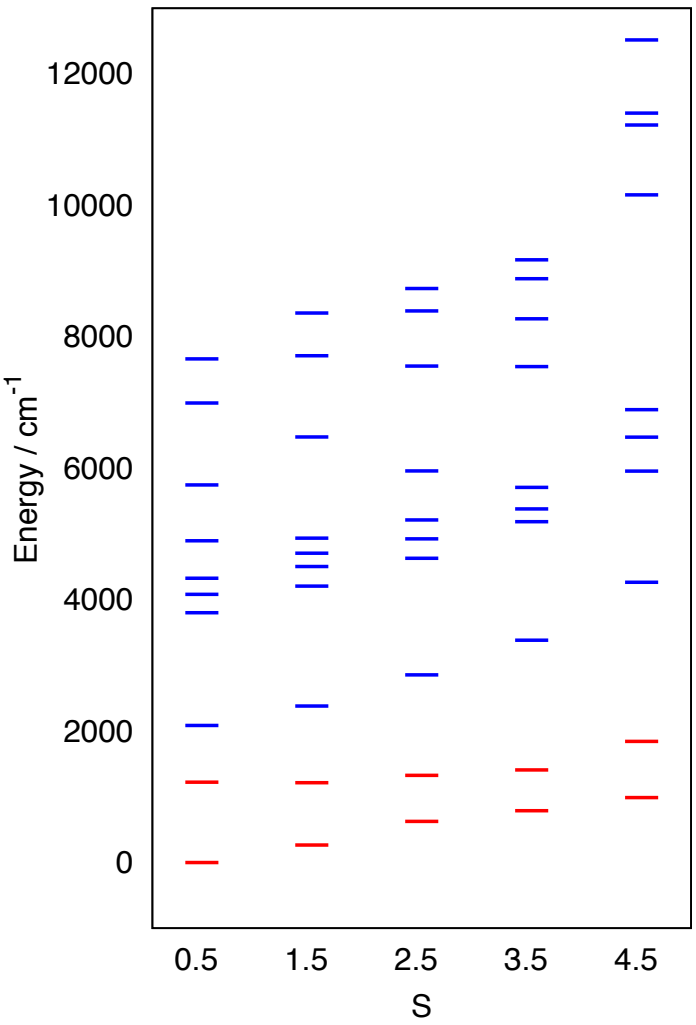

Supplementary Figure 4: The computed DMRG energy levels at the relaxed $[Fe_2S_2(SCH_3)_4]^{3-}$ dimer geometry.

double exchange and the need for the multi-orbital Anderson model hold quite generally.

2 4Fe-4S cluster

2.1 Geometry and orbitals

For the [4Fe-4S] cluster, we computed an optimized BS-DFT geometry using the BP86 functional and a triple zeta valence basis (TZV) basis set [16]. The optimized geometry is shown in Supplementary Table 11.

The active space orbitals are chosen in the same way as in the case of the [2Fe-2S] dimer. An unrestricted DFT BP86/SVP calculation was performed at the optimized geometry for the neutral [4Fe-4S] (all ferric) cluster in the high spin (S_z=10) state. The occupied and unoccupied alpha orbitals were then separately localized using the Pipek-Mezey localization technique. The 20 Fe 3d orbitals, 12 bridging S 3p orbitals, as well as 4 terminal ligand S 3p orbitals that point towards the Fe atoms, were identified by visual inspection. The occupancy of these orbitals in the $[Fe_4S_4(SCH_3)_4]^{2-}$ cluster gives an active space of (54e, 36o). Some representative orbitals in the active space are shown in Supplementary Figure 6.

2.2 DMRG calculations

2.2.1 Active spaces

The DMRG-CI calculation with an active space of (54e, 36o) is performed with a maximum of M=7500 spin-adapted renormalized states. The 36 orbitals include 20 Fe 3d orbitals, 12 bridging S 3p orbitals, as well as 4 terminal ligand S 3p orbitals that point towards the Fe atoms. For rapid convergence of DMRG energy these orbitals were were ordered as follows: S4($3p_5$), S10($3p_5$), Fe5(3d), Fe5(3d), Fe5(3d), Fe5(3d), Fe5(3d), S3($3p_5$), S1($3p_5$), S1($3p_6$), S4($3p_6$), Fe6(3d), Fe6(3d), Fe6(3d), Fe6(3d), Fe6(3d), S11($3p_6$), S2($3p_6$), S4($3p_7$), S2($3p_7$), Fe7(3d), Fe7(3d), Fe7(3d), Fe7(3d), Fe7(3d), S3($3p_7$), S9($3p_7$), S3($3p_8$), S1($3p_8$), Fe8(3d),

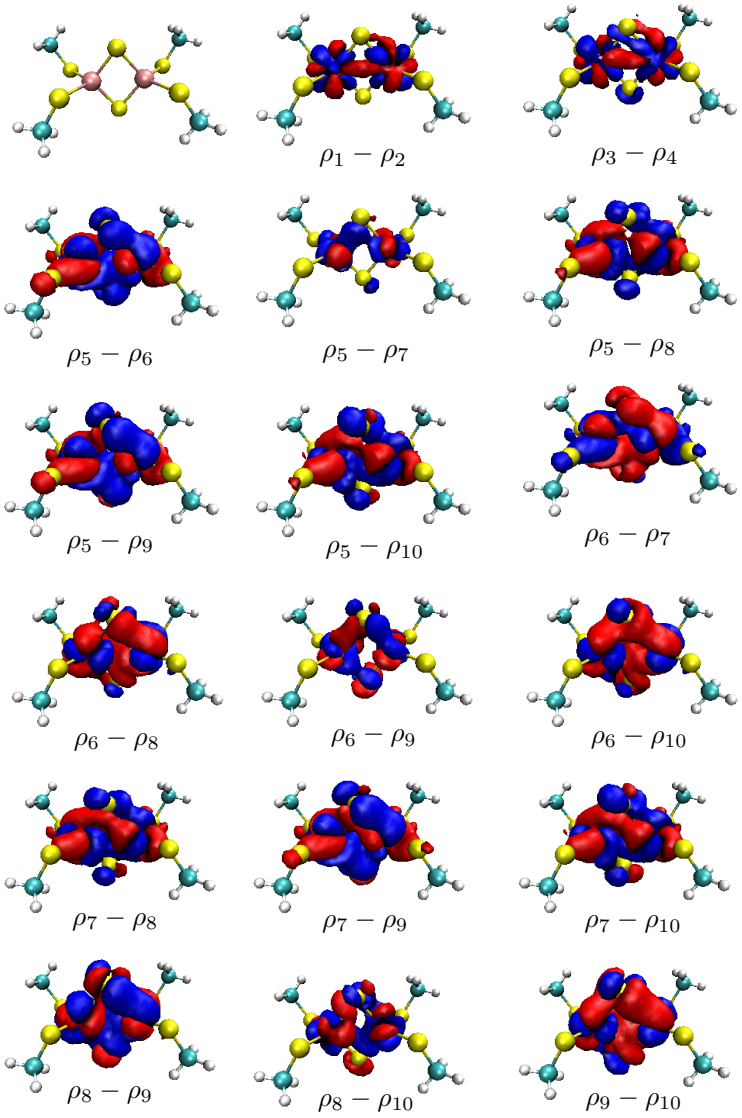

Supplementary Figure 5: Density differences between sets of doublet states in the $[Fe_2S_2(SCH_3)_4]^{3-}$ complex. We notice that besides the lowest two pairs of states, the density difference involves contributions from many d orbitals.

Supplementary Table 11: Coordinates (in Å) of the $[Fe_4S_4(SCH_3)_4]^{2-}$ model complex.

		x	y	z
1	S	0.04	-1.78	-1.29
2	S	-0.04	1.78	-1.29
3	S	1.78	-0.04	1.29
4	S	-1.78	0.04	1.29
5	Fe	0.05	-1.37	1.01
6	Fe	-1.38	0.05	-1.00
7	Fe	-0.05	1.38	1.00
8	Fe	1.37	-0.05	-1.01
9	S	0.24	3.30	2.14
10	S	-0.24	-3.29	2.14
11	S	-3.29	-0.24	-2.14
12	S	3.29	0.24	-2.14
13	C	-3.80	-1.84	-1.38
14	H	-3.91	-1.71	-0.29
15	H	-4.76	-2.17	-1.81
16	H	-3.03	-2.60	-1.56
17	C	3.80	1.83	-1.38
18	H	3.91	1.71	-0.29
19	H	4.76	2.16	-1.81
20	H	3.03	2.59	-1.55
21	C	-1.83	-3.80	1.38
22	H	-2.16	-4.76	1.81
23	H	-2.59	-3.03	1.55
24	H	-1.70	-3.91	0.29
25	C	1.84	3.80	1.38
26	H	2.17	4.76	1.81
27	H	2.60	3.03	1.56
28	H	1.71	3.91	0.29

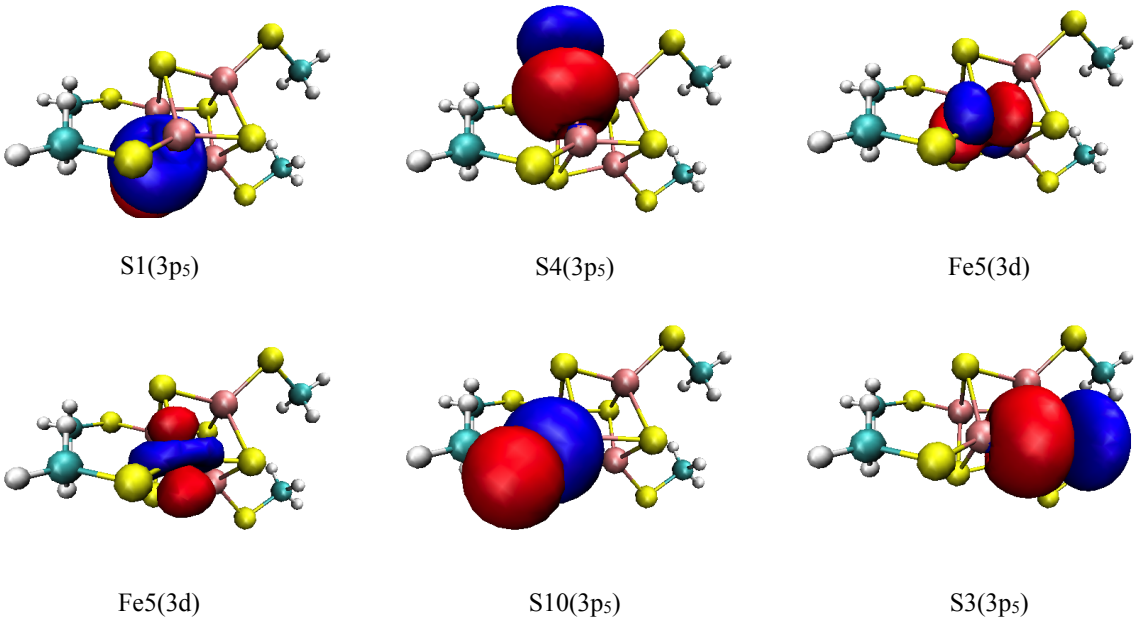

Supplementary Figure 6: Orbitals in the active space of the $[Fe_4S_4(SCH_3)_4]^{2-}$ cluster.

Fe8(3d), Fe8(3d), Fe8(3d), Fe8(3d), S2($3p_8$), S12($3p_8$), where the atom labels correspond to the labels in Supplementary Tables 11, and Supplementary Figure 1, and the subscript on S 3p orbitals is the index of the atom they are pointing towards.

2.2.2 Energy convergence

As mentioned in the main text of the article (see panel A of Supplementary Figure 5), in a perfect cubane cluster there are three equivalent pairings of the spins of the four Fe atoms to form a singlet ground state. In practice, structural distortion lifts this degeneracy, but the electronic distortion energy is quite small (associated with an energy scale of less than 8mE_h as seen in 7). This small energy difference can make robust convergence of the DMRG wave function to the true ground state difficult because the wavefunction optimization can get stuck early on in the "wrong" pairing. To expedite the convergence of the wave function towards the correct ground state the Hamiltonian is artificially perturbed so that atoms pairs (Fe5, Fe6)

and (Fe7, Fe8) gain a strong tendency to ferromagnetically align. This is done by artificially increasing the exchange integrals between the 3d orbitals of the paired up Fe atoms by 0.01 E_h until the number of renormalized states M=1600 is reached. Subsequently this perturbation in the Hamiltonian is decreased to zero over the next few sweeps, and the rest of the DMRG calculation (up to M=7500) is performed on the unperturbed Hamiltonian.

In fact, the above method of perturbing the Hamiltonian can be used to "converge" the DMRG wavefunction towards any of the three pairings shown in Supplementary Figure 5. The ground-state pairing is identified as the one with the lowest energy. The other pairings do not necessarily approximate exact eigenstates of the full Hamiltonian, but rather, are local minima in the parameter space of DMRG. They are a form of "broken-symmetry" DMRG solution, and can be thought of as the best DMRG states that can be obtained with a maximum M=7500, when the spin couplings of the various Fe centers is constrained to be non-optimal. The energy differences between these different solutions can be used to estimate the difference in the exchange coupling coefficients of the HDE model hamiltonian (see Section 2.4).

The DMRG energies and discarded weights at different values of M are used to extrapolate to zero discarded weight, which also gives us the estimated energy errors. This is shown in Supplementary Figure 7. Our estimated error in the total energies is less than 1 mE_h.

2.3 Local charge and spin

Local populations and spin correlation functions between different Fe atoms 1-4 can be calculated using the equations 1 and 2 and are given in Supplementary Table 12.

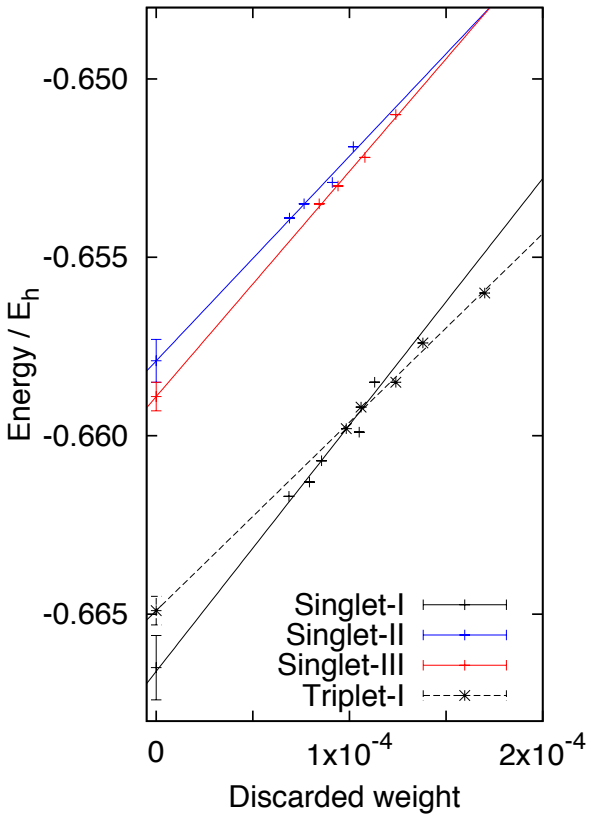

Supplementary Figure 7: DMRG energy (E+8471.0) in E_h of the ground-state singlet (Singlet-I) and triplet (Triplet-I) states versus the discarded weight of the $[Fe_4S_4(SCH_3)_4]^{-2}$ cluster. In addition, the energies of Singlet-II and Singlet-III correspond to the states where the spin pairing is constrained be non-optimal (see text). The best fit straight lines are extrapolated to zero discarded weight, with the shown error bars, to obtain an estimated FCI energy.

Supplementary Table 12: Local population and spin correlation function for the four Fe atoms in the calculated DMRG states of the $[Fe_4S_4(SCH_3)_4]^{-2}$ cluster.

Fe atom	$\langle N_i \rangle$	$\langle S_i \cdot S_j \rangle$			
		Fe1	Fe2	Fe3	Fe4
Singlet-I					
Fe1	6.27	5.27	3.24	-4.05	-4.05
Fe2	6.27	3.24	5.26	-4.05	-4.04
Fe3	6.27	-4.05	-4.05	5.27	3.24
Fe4	6.27	-4.05	-4.04	3.24	5.27
Singlet-II					
Fe1	6.25	5.32	-4.03	3.30	-4.18
Fe2	6.26	-4.03	5.32	-4.18	3.30
Fe3	6.26	3.30	-4.18	5.32	-4.03
Fe4	6.25	-4.18	3.30	-4.03	5.32
Singlet-III					
Fe1	6.25	5.32	-4.06	-4.18	3.31
Fe2	6.25	-4.06	5.33	3.32	-4.17
Fe3	6.25	-4.18	3.32	5.33	-4.06
Fe4	6.25	3.31	-4.17	-4.06	5.32
Triplet					
Fe1	6.26	5.29	3.22	-3.77	-3.77
Fe2	6.26	3.22	5.27	-3.95	-3.95
Fe3	6.26	-3.77	-3.95	5.28	3.26
Fe4	6.26	-3.77	-3.95	3.26	5.28

2.4 Model Hamiltonian for pairing and unequal exchange in the [4Fe-4S] cluster

2.4.1 Single orbital Anderson model

The direct extrapolation of the simple (single orbital per Fe) Anderson model described in Eq. (4) to the case of [4Fe-4S] cluster takes the form

$$H = \sum_{ij} J_{ij}(S_i \cdot S_j + S_i \cdot s_j + S_j \cdot s_i) + \sum_{\sigma=\uparrow,\downarrow} \beta_{ij}(c^{\dagger}_{i\sigma}c_{j\sigma} + c^{\dagger}_{j\sigma}c_{i\sigma}) \tag{8}$$

with 6 Heisenberg coupling coefficients J_{ij} and 6 hopping integrals β_{ij}. We assume that there are two hopping electrons, and that the two electrons cannot be on the same Fe atom due to on-site repulsion.

We solve the above Hamiltonian numerically in the space where the spins s_i and $S_i = 5/2$ are anti-ferromagnetically aligned. The nature of the states changes as the ratio of the exchange coupling coefficients changes. In Supplementary Figure 8 we take $B = 2J'$ and $J_{12}, J_{34} = J'$, $J_{13}, J_{14}, J_{23}, J_{24} = J$. For $J/J' > 1.2$, we recover a single pairing picture for the S_{12}=9/2 dimer states that is assumed in the generalized HDE model of Noodleman et al. [17, 18, 19, 20, 21].

The difference in the J_{ij} parameters can be estimated from energy differences between the ground state singlet and triplet states and the difference between the ground state singlet state (Singlet-I) and artificially paired singlet (Singlet-II). The energy difference between the singlet and the triplet state is given by

$$E(S) - E(T) = J - 0.08|B| \tag{9}$$

and the energy difference between Singlet-I and Singlet-II states is given by

$$E(S_I) - E(S_{II}) = 22.5(J - J') \tag{10}$$

In Eq. 9 we assume $B = J$ so that the singlet-triplet gap is $0.92J$. In Eq. 10 we have assumed that difference in the value of B for different couplings is relatively small. Using the converged

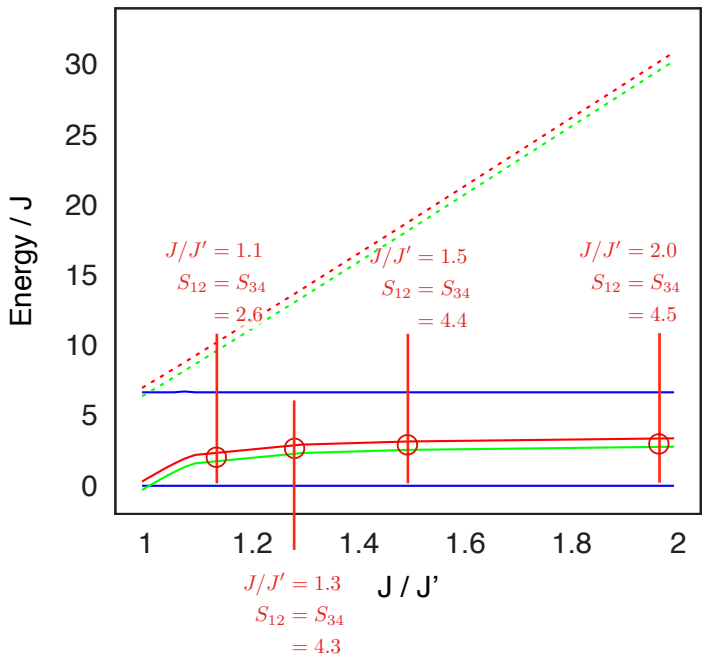

Supplementary Figure 8: Simplified Anderson model energy levels for the [4Fe-4S] cluster, as a function of anisotropic exchange $J' \neq J$. As the anisotropy increases, we recover the fixed-pairing picture assumed by the HDE model.

DMRG energies we obtain $J = 382$ cm^{-1} and $J - J' = 84$ cm^{-1}, from which we conclude that $J/J' \approx 1.28$ and the [4Fe-4S] low-lying states with high effective dimer spin can be described by the single pairing picture, although they appear to lie close to the border of validity of that description.

2.4.2 Multi-orbital Anderson model

To check that the above analysis holds in the more complex case of multi-orbital double exchange, we have also analyzed some multi-orbital (per Fe) Anderson models for the [4Fe-4S] cluster. These take the form

$$H = \sum_{iAB} J_{iAB} s_{iA} \cdot s_{iB} + \sum_{iAB\sigma} \beta_{iAB} (c^\dagger_{iA\sigma} c_{iB\sigma} + c^\dagger_{iB\sigma} c_{iA\sigma}) + \sum_{iA\sigma} \Delta_{iA} c^\dagger_{iA\sigma} c_{iA\sigma} \qquad (11)$$

where A and B now range over the 4 Fe atoms. The index i ranges over the number of d orbitals on each Fe atom. This would be 5 orbitals in the real cubans, but solving the Hamiltonian for all its levels would be prohibitively expensive. We have therefore considered simpler versions (which illustrate the appropriate trends) where each model Fe atom has respectively only 1 or 2 orbitals. Note that in the 1 orbital case, the maximum spin on each Fe is then only 1/2, and the maximum dimer spin is also 1/2, while in the 2 orbital case, the maximum spin on each Fe is 1 and the maximum dimer spin is 3/2. (The 1 orbital model is related to the Hubbard model on a tetrahedron as discussed in Refs. [22]). In Supplementary Figures 9 and 10 we plot the effective dimer spins of the energy levels as a function of the exchange couping ratio (inequivalent J's), for $\beta_{iAB} = 2J'$ and $\Delta_{iA} = 0$ (for all i, A). We see the same general trends as in the simple Anderson model above. Note that J_c shifts to lower values as the number of orbitals on each Fe increases.

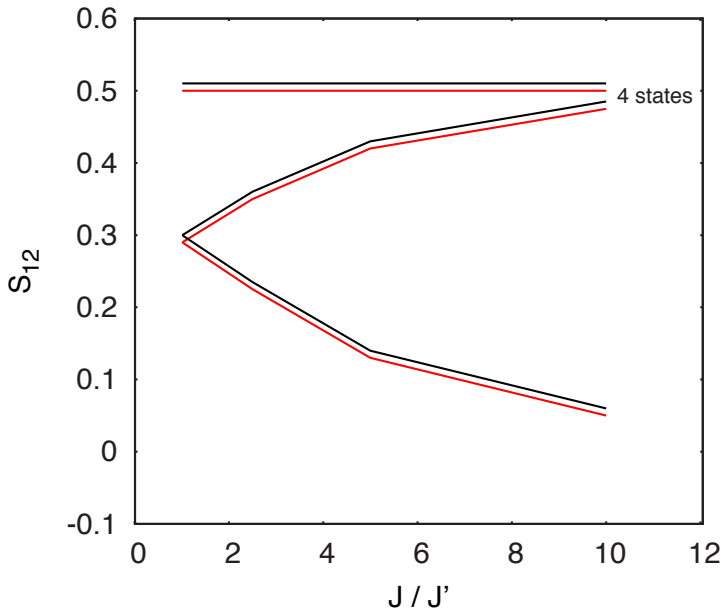

Supplementary Figure 9: Effective dimer spins of the energy levels as a function of exchange coupling ratio for the [4Fe-4S] multi-orbital Anderson model with 1 orbital per model Fe atom. Note that since the "Fe" atom has only one orbital, the maximum spin per atom is 1/2, and the maximum dimer spin is 1/2.

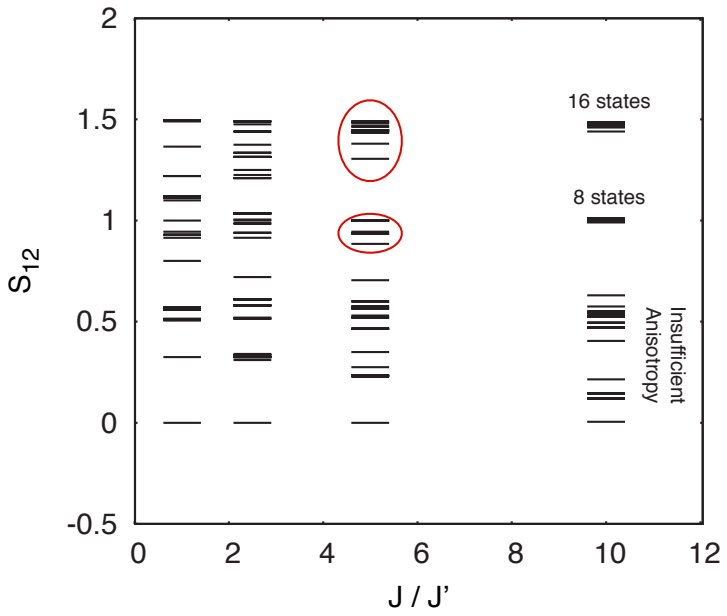

Supplementary Figure 10: Effective dimer spins of the energy levels as a function of exchange coupling ratio for the [4Fe-4S] multi-orbital Anderson model with 2 orbitals per Fe. Note that since the "Fe" atom has only two orbitals, the maximum spin per atom is 1, and the maximum dimer spin is 3/2.

References

[1] J. J. Mayerle, S. E. Denmark, B. V. DePamphilis, J. A. Ibers, R. H. Holm, *Journal of the American Chemical Society* **97**, 1032 (1975).

[2] A. Schafer, H. Horn, R. Ahlrichs, *J. Chem. Phys.* **97**, 2571 (1992).

[3] F. Neese, *Wiley Interdisciplinary Reviews: Computational Molecular Science* **2**, 73 (2012).

[4] L. Bytautas, J. Ivanic, K. Ruedenberg, *The Journal of Chemical Physics* **119**, 8217 (2003).

[5] J. Pipek, P. G. Mezey, *The Journal of Chemical Physics* **90**, 4916 (1989).

[6] S. Sharma, G. K.-L. Chan, *The Journal of Chemical Physics* **136**, 124121 (2012).

[7] K. Andersson, B. O. Roos, *Chemical Physics Letters* **191**, 507 (1992).

[8] G. K.-L. Chan, M. Head-Gordon, *The Journal of Chemical Physics* **118**, 8551 (2003).

[9] E. Ramos-Cordoba, E. Matito, I. Mayer, P. Salvador, *Journal of Chemical Theory and Computation* **8**, 1270 (2012).

[10] K. Yamaguchi, T. Fueno, *Chemical Physics* **19**, 35 (1977).

[11] K. Yamaguchi, *Chemical Physics* **29**, 117 (1978).

[12] P. W. Anderson, H. Hasegawa, *Physical Review* **100**, 675 (1955).

[13] L. Noodleman, E. J. Baerends, *Journal of the American Chemical Society* **106**, 2316 (1984).

[14] M. Shoji, *et al.*, *International Journal of Quantum Chemistry* **107**, 609 (2007).

[15] J. Rawlings, O. Siiman, H. B. Gray, *Proceedings of the National Academy of Sciences* **71**, 125 (1974).

[16] F. Weigend, R. Ahlrichs, *Phys. Chem. Chem. Phys.* **7**, 3297 (2005).

[17] L. Noodleman, C. Y. Peng, D. A. Case, J. M. Mouesca, *Coordination Chemistry Reviews* **144**, 199 (1995).

[18] K. Yamaguchi, Y. Yoshioka, T. Takatsuka, T. Fueno, *Theoretica chimica acta* **48**, 185 (1978).

[19] K. Yamaguchi, T. Fueno, N. Ueyama, N. Akira, O. Masaaki, *Chemical Physics Letters* **164**, 210 (1989).

[20] Y. Kitagawa, *et al.*, *International Journal of Quantum Chemistry* **108**, 2881 (2008).

[21] M. Nishino, *et al.*, *Bulletin of the Chemical Society of Japan* **71**, 99 (1998).

[22] L. Falicov, R. Victora, *Physical Review B* **30**, 1695 (1984).